Acta Materialia 269 (2024) 119795

Contents lists available at ScienceDirect

Acta Materialia

journal homepage: www.elsevier.com/locate/actamat

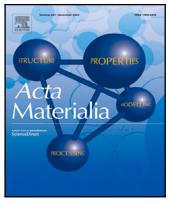

Full length article

Kinetic Monte Carlo simulations of solute clustering during quenching and aging of Al–Mg–Zn alloys

Zhucong Xi [a], Louis G. Hector Jr. [b], Amit Misra [a], Liang Qi [a,*]

[a] Department of Materials Science and Engineering, University of Michigan, Ann Arbor, MI, 48109, USA
[b] GM Global Technical Center, General Motors Company, Warren, MI, 48092, USA

ARTICLE INFO

Keywords:
Kinetic Monte Carlo simulations
Solute clustering
Al–Mg–Zn alloys
Quenching
Natural aging

ABSTRACT

The physical mechanisms behind cluster formation during quenching and aging of age-hardening metallic alloys are poorly understood based on classical nucleation and growth theories, especially in multicomponent alloys with supersaturated vacancies and fast-diffusing solute atoms. Here, solute clustering in an Al–Mg–Zn alloy during quenching immediately after high-temperature (800 K) solution treatment is modeled with a newly developed kinetic Monte Carlo (kMC) framework. This includes accurate surrogate models trained using first-principles-calculated data to predict vacancy migration energetics on the fly as functions of local lattice occupations. First, kMC simulations at constant aging temperatures revealed that temporal evolution of the number, sizes, and compositions of solute clusters change with aging temperature. Such changes are consistent with our analyses based on classical nucleation theory (CNT) and Monte Carlo simulations. Second, the kMC algorithm was revised for simulating quenching processes by iteratively updating the kMC temperature based on simulated cooling rate profiles. These quenching simulations show that rapid solute clustering mainly occurs from ~600 to ~400 K during cooling. Below ~400 K, the clustering is suppressed to a steady state because vacancies are trapped by stable clusters with sizes of ~2 nm and high magnitudes of formation energies. The configurations of these steady-state clusters closely resemble the solute clusters we observed experimentally in 7XXX series Al–Mg–Zn-based alloy samples immediately after quenching. A two-stage vacancy trapping mechanism revealed in our simulations can provide physical guidance to tune precipitation kinetics during natural and artificial aging.

1. Introduction

The successful processing and application of advanced age-hardening metallic alloys necessitate a profound understanding and delicate manipulation of the intricate precipitation kinetics [1]. As demonstrated in many examples [2–5], the classical nucleation theory (CNT) emerges as a pivotal and robust framework to interpret and predict the nucleation and growth rates of precipitates observed in both experiments and simulations. Despite their wide applicability, CNT faces challenges under extreme and complex conditions. For example, complicated chemical environments in multi-component alloys [6–9] may present obstacles in accurately estimating critical free energy barriers. Vacancy trapping mechanisms [10–12] may also significantly change vacancy migration energetics to greatly change the diffusion kinetics. These special conditions often appear in the nucleation and early growth stages of the multistep precipitation kinetics during the thermomechanical processing of age-hardening multi-component alloys [13]. To bridge this gap, we propose a kinetic Monte Carlo (kMC) simulation framework based on accurate models of vacancy migration energetics. To demonstrate its capability to deal with the complex conditions mentioned above, we apply this framework to investigate solute clustering starting from a solid solution state in an Al–Mg–Zn alloy, which has the chemical composition of commercial 7XXX series Al alloys, at constant temperatures and during quenching.

The 7XXX series Al alloys, which were originally designed for aerospace applications, possess a remarkable specific strength when in peak-aged condition with yield strengths usually ranging from 470 to 570 MPa [14]. For some special 7XXX series Al alloys, such as 7068, yield strengths of up to 700 MPa in the T6 temper (solution heat-treated and artificially aged) are possible [15]. Extensive use of 7XXX series Al in the automotive industry, especially in body structure components of automobiles and trucks, can significantly contribute to the goal of creating lightweight vehicles, thereby contributing to greenhouse gas reduction. However, there are challenges associated

* Corresponding author.
E-mail address: qiliang@umich.edu (L. Qi).

https://doi.org/10.1016/j.actamat.2024.119795
Received 10 September 2023; Received in revised form 30 January 2024; Accepted 24 February 2024
Available online 1 March 2024

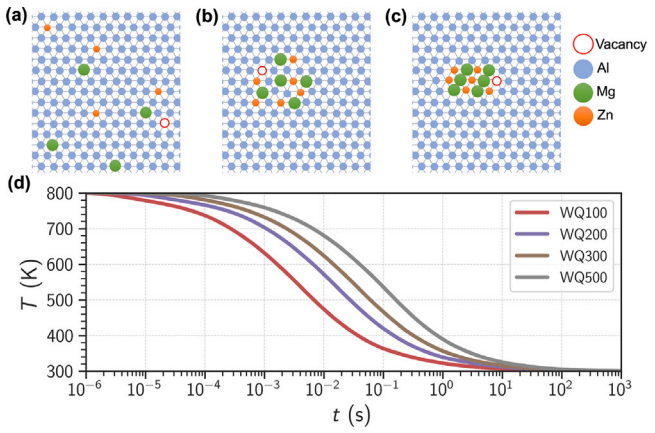

Fig. 1. Schematic plots of our focused phase transformation and the corresponding temperature evolution profiles. (a)–(c): Illustrations of solute clustering kinetics in Al–Mg–Zn-based alloys after solid-solution treatments. (a) Supersaturated solid solution (SSSS), (b) solute-rich clusters (SRC), and (c) Guinier-Preston (GP) zones (nanoscale coherent Mg/Zn-rich clusters). (d) Simulated temperature evolution profiles over time during water quenching (WQ) at different quenching rates from 800 K to 300 K for Al samples with varying thicknesses. The number following WQ denotes sample thickness measured in μm.

with the formability of automotive applications due to rapid natural aging [16–18].

A comprehensive summary of high-temperature forming processes for high-strength aluminum alloys can be found in the recent review [19]. Therefore, we will briefly summarize key issues here. Aluminum sheet alloys are typically subjected to a solutionizing heat treatment prior to conventional mechanical forming processes such as stamping and hemming. This is followed by room-temperature forming of the sheet material in the as-quenched state when it is highly ductile and finally followed by artificial aging during paint bake. During natural aging at room temperature, however, the nucleation of solute clusters and early-stage precipitates can occur fast (often within 30 min after quenching) for current 7XXX series Al alloys. Consequently, room temperature formability of these alloys decreases very rapidly, necessitating warm or hot stamping wherein solutionizing-quenching occurs in a narrow time window [20–27]. The decrease in formability, along with changes in other mechanical properties, such as the gradual increase in strength and hardness, are strongly influenced by factors including the aging temperature and time as well as cooling rates [28–32] during sheet processing.

The changes in mechanical properties, while macroscopic in nature, have underlying atomistic-scale origins. They are closely related to the evolution of the atomistic structures of precipitates [33–36]. Consequently, understanding and controlling the nucleation and early stages of precipitation kinetics can guide future 7XXX alloy designs that have improved formability without compromising mechanical properties [28,37–39]. A first step towards this is the understanding of nucleation and growth of precipitates in Al–Mg–Zn-based alloys. This is currently understood to proceed as follows [34,39–43]: supersaturated solid solution (SSSS, Fig. 1(a)) → solute-rich clusters (SRC, Fig. 1(b)) → Guinier-Preston(GP) zones (nanoscale coherent Mg/Zn-rich clusters, Fig. 1(c)) → metastable η' (semi-coherent Mg–Zn–Al precipitates with high Zn/Mg ratio) → stable η (incoherent $MgZn_2$). During natural aging, the majority of precipitates are SRC and GP zones, even though η' may occur in some cases [35,44]. Many studies have been performed to understand the latter stages of this precipitation sequence starting from the nanoscale GP zones to η' and η precipitates [29,41,45–48]. However, due to the fast time scale (within seconds) of nucleation kinetics and small length scales (within nanometers) of solute clusters, the initial stages of this precipitation sequence from the solid solutions to the GP zones have not been clarified.

There exist many theoretical studies and kMC simulations on solute clustering processes starting from solid solution stages at constant temperatures for both natural aging (~ 300 K) and artificial aging (~ 450 K) conditions [3,38,49–53]. However, our recent *in situ* transmission electron microscopy (TEM) observations show that solute clusters with diameters of ~2 nm were observed immediately after quenching from the solutionizing temperatures (~ 800 K) [13], indicating early-stage phase transformations during the short quenching process. CNT for precipitates is usually utilized to analyze phase transformations at constant temperatures or conditions with slowly varying temperatures [2–5,54,55], which are not suitable for understanding solute clustering that occurs during fast quenching processes.

In this paper, solute clustering, starting from a random solid-solution state in an Al–Mg–Zn alloy, is simulated with a newly developed kMC framework, whose details are explained in Section 2. Accurate surrogate models are constructed using first-principles data to predict vacancy migration energy barriers and corresponding energetic driving forces on the fly as a function of the local lattice occupations in the Al FCC lattice [9]. These models are implemented in kMC simulations to quantify solute clustering kinetics both at constant temperatures (650 K, 500 K, and 300 K) and during quenching processes (from 800 K to 300 K) based on a revised kMC algorithm. The temperature profiles of the quenching process were obtained from COMSOL Multiphysics simulations [56]. As shown in Fig. 1(d), 'WQ' curves indicate the cooling rate of water quenching for samples with varying thicknesses, with the number following WQ denoting the material thickness in μm. These temperature profiles show that quenching processes are typically completed within several tens of seconds, and it only takes less than 1 s for the temperature to drop from 800 K to 400 K. Additionally, to confirm the mechanisms of solute clustering kinetics, we built the free-energy landscape of Mg–Zn-rich solute clusters as a function of the numbers of Mg and Zn atoms in an Al–Mg–Zn alloy and applied the energy landscape to our CNT model, which can help us to estimate the nucleation rates and the cluster composition changes during the early nucleation stages at different temperatures. After the initial nucleation stage, to assist the analyses of the thermodynamic driving forces for further cluster growths and the related structural/composition variations, we also performed time-independent canonical Monte Carlo (CMC) simulations at different temperatures to study the properties of solute clusters under thermodynamically equilibrium conditions for the same Al–Mg–Zn alloy.

As described in the upcoming Section 3, our kMC results at constant temperatures reveal that relatively large-size and high-density solute clusters are generated at an intermediate temperature (500 K) relative to those obtained from either high-temperature (650 K) or room-temperature (300 K) kMC simulations. This trend is also confirmed by our CNT model for Mg–Zn-rich clusters, which shows that intermediate temperature has the largest nucleation rates. Additionally, the solute clusters from kMC exhibit different distributions of Zn/Mg ratios and other properties as the temperature varies. Meanwhile, our CMC simulations reveal a solute cluster phase transformation as the temperature drops below a critical temperature of ~400 K, which shows different solute cluster compositions and lattice occupation ordering below and above the critical temperature, consistent with the trends observed in our kMC simulations at constant temperatures. For quenching process simulations based on our revised kMC algorithm, the rapid solute clustering kinetics occurs at intermediate temperatures (from ~600 to ~400 K). As the temperature goes down to a critical value (~ 400 K), the solute clustering kinetics is suppressed to reach a steady state because the vacancies are trapped by stable clusters with sizes of 1~2 nm and high average formation energies. The statistical features of number, sizes, energetics, and chemical compositions of solute clusters at the steady state depend on the cooling rate of the temperature profiles shown in Fig. 1(d). These steady-state clusters have configurations (sizes and densities) similar to the solute clusters observed immediately

after quenching in our *in situ* TEM characterizations [13]. The impacts of these results, on the aspects of nucleation/growth theories, especially the vacancy trapping mechanisms [10–12], and age-hardening processing techniques for the desired mechanical properties of Al alloys, are discussed and summarized in Section 4.

2. Methods

The kMC simulations were conducted to simulate solute atom diffusion based on vacancy migrations in a coherent FCC lattice. As confirmed by our recent *in situ* TEM observations [13], the coherent lattice assumption is reasonable as our focus is exclusively on solute clusters and early-stage precipitates. In these kMC simulations, the key input is a numerical function to describe the activation energy barrier along the minimum energy path (MEP) for the vacancy migration at a particular local lattice occupation environment as described in Section 2.1. The detailed kMC algorithms, including the algorithm to bypass flicker events, are described in Section 2.2. We also provide details of our time-independent canonical Monte Carlo simulations to simulate the thermodynamics of solute clusters in the FCC lattice in Section 2.4. Finally, a revised kMC algorithm to simulate the clustering kinetics during a quenching process is described in Section 2.5.

2.1. Surrogate models for vacancy migration energetics

We first apply surrogate models that use lattice occupations as inputs to predict the following energetic values: the total energy E_{tot} of a lattice occupation configuration in a supercell, the energy landscape E_{MEP} of the minimum energy path (MEP) as a function of the reaction coordinate x for the vacancy migration, and the critical energetic parameters of vacancy migration, such as energetic driving forces ΔE and vacancy migration energy barriers ΔE_{a}. The surrogate models were trained based on density functional theory (DFT) calculations from our previous work [9], where 1250 MEPs were calculated via DFT calculations plus the climbing image nudged elastic band (CI-NEB) method [57–59], so 2500 ΔE and ΔE_{a} pairs (plus the corresponding supercell configurations of the initial and final states and their energies E_{tot}) were collected by considering both forward and backward vacancy migrations. To train the surrogate models for E_{tot}, ΔE, and ΔE_a, 2000 training data points were chosen randomly from the total 2500 data points generated from the DFT+CI-NEB calculations. The remaining 500 were reserved as testing data to evaluate the predictive accuracy of the surrogate models.

The surrogate model to predict E_{tot} of a lattice occupation configuration was guided by the cluster expansion method [53,60–62]. The input information was chosen to be the atom types on all lattice sites in the lattice occupation configuration, $\bar{\sigma}_{\text{config}}$. We employed the one-hot encoding method [63,64] to represent site occupation, eliminating any quantitative relationship of variables compared to giving each site a scalar index. The total energy E_{tot} was expressed using the number of different types of clusters, ϕ_α, and their effective cluster interactions (ECI), J_α. Only clusters of no more than three atoms (any two atoms in one cluster have their distance no more than the third nearest neighbor distance) were considered. See Supplementary Note 1 for details of the surrogate model for the prediction of E_{tot}.

The surrogate model to predict MEPs was adopted from our previous work [9], where we found that the MEP of vacancy migration is greatly affected by local lattice distortions. We proposed that the MEP can be expressed as a quartic function, $E_{\text{MEP}}(x) = ax^4 + bx^3 + cx^2$, as shown in Fig. 2(a), where E_{MEP} is the energy landscape of the MEP as a function of the reaction coordinate x. Here, the coefficients (a, b, and c in the quartic function for E_{MEP}) depend on the local lattice distortions introduced by different occupations on the sites near the vacancy and the migration atom. The energy landscape has a transition state (x_{T}) at a local maximum and the initial state (x_{I}) and final state (x_{F}) at two local minima. Thus, the critical MEP properties, such as $\Delta E_a = E_{\text{MEP}}(x_{\text{T}}) - E_{\text{MEP}}(x_{\text{I}})$, $\Delta E = E_{\text{MEP}}(x_{\text{F}}) - E_{\text{MEP}}(x_{\text{I}})$, can be quantified. To unify our energetic surrogate models and ensure accuracy at both short-range distances and long-range distances, we calculate the MEP ΔE by directly taking the difference between $E_{\text{MEP}}(x_{\text{F}})$ and $E_{\text{MEP}}(x_{\text{I}})$, which are both predicted using the aforementioned surrogate model of the total energy E_{tot}. For the prediction of other MEP properties such as ΔE_a, the input was the type of the migrating atom and the type of all atoms on the 1st, 2nd, and 3rd nearest-neighbor lattice sites relative to the vacancy/migration atom, $\bar{\sigma}_{\text{neighbor}}$. See Supplementary Note 2 for details of the surrogate model for MEP prediction.

The performance and accuracy of surrogate models are validated through comparison with DFT+CI-NEB calculations. First, the prediction of ΔE was evaluated by taking the difference of the predicted E_{tot} at the initial and final states of the given lattice occupation configurations. Fig. 2(b) demonstrates a comparison between predicted ΔE (X-axis) and that derived from DFT calculations (Y-axis) with a low root-mean-square error (RMSE) of 0.0492 eV and a robust coefficient of determination (R^2) score of 73.5%. In addition, the performance in predicting MEP ΔE_a was examined as displayed in Fig. 2(c). It compares ΔE_a from our surrogate model (X-axis) and DFT+CI-NEB methods (Y-axis) with the RMSE of 0.0507 eV and a high R^2 score of 91.50%, suggesting that the surrogate models are accurate enough for ΔE_a prediction. The relative low R^2 score for the ΔE predictions is related to the relatively small range of ΔE, which is mainly distributed from ~-0.2 eV to ~0.2 eV as shown Fig. 2(b). On the other hand, the distribution of ΔE_a is much wider from ~0.0 eV to ~1.2 eV, showing strong fluctuations of ΔE_a due to lattice distortion effects [9], so its R^2 score is much higher with almost the similar RMSE value compared with the counterparts of the ΔE surrogate model.

2.2. KMC algorithms

kMC simulations were employed to quantify solute clustering kinetics by vacancy migration in an FCC lattice of an Al–Mg–Zn alloy [51]. The most common approach to kMC simulations is the first-order residence time algorithm [65]. In this algorithm, the residence time of each kMC step is determined by the current state and one reaction path to a stochastically selected new state. The name 'first-order' is derived from the fact that the transition to the new state can only be reached by a one-step reaction path. Since atomic diffusion is mediated by vacancy migrations, we can start by considering a vacancy surrounded by z nearest neighbors. Each neighboring atom of the vacancy is vibrating around its lattice position with a frequency ν_i. This frequency is chosen to be 1×10^{13} Hz as a typical atomic vibration frequency value in a crystal. For the neighboring atom i, the transition probability per unit time for this atom jumping to the vacancy is $r_i = \nu_i \exp(-\frac{E_a^i}{k_B T})$, where E_a^i is the vacancy migration energy barrier (the same meaning as ΔE_a shown in Fig. 2(a)), and k_B and T denote Boltzmann constant and temperature, respectively. Thus, the relative probability that the vacancy will jump to any one of its nearest neighbors is

$$p_i^{(1)} = \frac{r_i}{\sum_i r_i} \tag{1}$$

where the summation accounts for all potential jumps to the z nearest neighbors.

To determine to which nearest neighbor the vacancy jumps, a random number between 0 and 1 is uniformly generated, $\xi_1 \sim \mathcal{U}(0,1)$. The vacancy jump to the site m is selected at this kMC step if $\sum_{i=1}^{m-1} p_i^{(1)} < \xi_1 \leq \sum_{i=1}^{m} p_i^{(1)}$. One-step residence time of this kMC step then can be expressed as $\Delta t = -\frac{\ln \xi_2}{\sum_i^z r_i}$, where $\xi_2 \sim \mathcal{U}(0,1)$ is generated from another uniform random variable between 0 and 1. The ensemble expectation of a time step of the first-order kMC algorithm is expressed as

$$\Delta \bar{t}^{(1)} = \frac{1}{\sum_i r_i} \tag{2}$$

For some alloy systems, such as the Al–Mg–Zn, E_a^i can be greatly affected by the chemical species around the vacancy due to local lattice

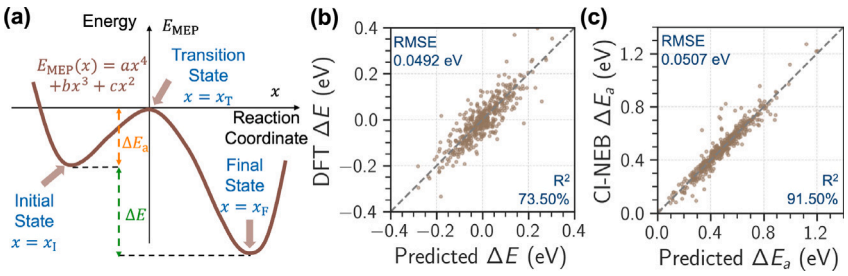

Fig. 2. Surrogate models to predict minimum energy paths (MEP) and critical energetic parameters for a general vacancy migration event to its first nearest neighbor in the FCC lattice of Al–Mg–Zn alloys [9]. (a): Schematic plot of the MEP of vacancy migration showing the migration energy barrier ΔE_a and energy driving force ΔE by using a quartic function to describe the MEP energy evolution E_{MEP} as a function of the reaction coordinate x. (b)–(c): Performance of surrogate models to predict ΔE (b) and ΔE_a (c) for the testing data set in Al–Mg–Zn alloys by comparisons with those from first-principles DFT+CI-NEB calculations. In (b) and (c), the root-mean-square error (RMSE) is denoted at the upper left, and the number at the bottom-right corner shows the coefficient of determination (R^2).

distortion [9]. For some local lattice occupations, the vacancy and one of its adjacent solute atoms are close to each other due to strong lattice distortion, resulting in small values of E_a^i for both the forward and backward jump of the vacancy. Thus, after the vacancy exchanges the position with an adjacent atom, there is a high probability for the vacancy to jump back to its previous position. These so-called 'flicker' events can greatly slow down the efficiency of the first-order algorithm, especially at low temperatures. Thus, the second-order residence time algorithm [66–68] was also applied to accelerate the kMC simulations by significantly minimizing flicker events.

The second-order algorithm considers two-step defect jumps, so it bypasses flicker events and calculates the exiting time directly. We denote the current state as k, the previous state as j, the next state as i, and the second next state as l. The exit time of state k using the first-order algorithm is $\vec{t}_k^{(1)} = \frac{1}{\sum_i r_{ki}}$, and that of state i is $\vec{t}_i^{(1)} = \frac{1}{\sum_l r_{il}}$. Here, we denote the normalized probability for a vacancy to jump from k to state i is p_{ki}, and the probability the vacancy jumps directly back to k from i as p_{ik}, both of which can be calculated by applying the first-order algorithm. Hence, the probability of this flicker jump is $\beta_{ki}^{b} = p_{ki}p_{ik}$, where the letter 'b' denotes that the vacancy jumps backward. The probability the vacancy does not jump back is $\beta_{ki}^{f} = p_{ki}(1 - p_{ik})$, where the letter 'f' denotes that the vacancy jumps forward. Correspondingly, the probability that a flicker happens is $\beta_k^{b} = \sum_i \beta_{ki}^{b}$ and the probability that a flicker does not happen is $\beta_k^{f} = \sum_i \beta_{ki}^{f}$. A jump from k to j is also considered a flicker, hence, we denote the jump from k to $i = j$ as an indirect move, and k to $i \neq j$ as a direct move. The probabilities of the indirect move and the direct move are:

$$p_i^{(2)} = \begin{cases} \frac{\beta_{kj}^{f}}{1-p_{kj}} \frac{\gamma_{kj}^{b}}{\beta_k^{f}} & \text{for } i = j \\ \frac{\beta_{ki}^{f}}{1-p_{kj}} \left(1 + \frac{\gamma_{kj}^{b}}{\beta_k^{f}}\right) & \text{for } i \neq j \end{cases} \tag{3}$$

where $\gamma_{kj}^{b} = \sum_{i \neq j} \beta_{ki}^{b}$. Similar to the first-order algorithm, a uniformly generated random number between 0 and 1, denoted as $\xi_1 \sim \mathcal{U}(0,1)$, is applied. The vacancy jump to the site m is selected at this kMC step if $\sum_{i=1}^{m-1} p_i^{(2)} < \xi_1 \leq \sum_{i=1}^{m} p_i^{(2)}$. The ensemble expectation of a single jump's timestep is

$$\Delta\vec{t}^{(2)} = \frac{1}{1-p_{kj}} \left[\gamma_{kj}^{f} \vec{t}_k^{(1)} + \gamma_{kj}^{b} \left(\vec{t}^{(1)} + t_{sj} + \frac{\beta_k^{b}}{\beta_k^{f}} t_s\right)\right] \tag{4}$$

where $\gamma_{kj}^{f} = \sum_{i \neq j} \beta_{ki}^{f}$, $t_{sj} = \frac{1}{\gamma_{kj}^{b}} \sum_{i \neq j} \left[\left(\vec{t}_k^{(1)} + \vec{t}_i^{(1)}\right) \beta_{ki}^{b}\right]$, and $t_s = \frac{1}{\gamma_{kj}^{b}} \sum_i \left[\left(\vec{t}_k^{(1)} + \vec{t}_i^{(1)}\right) \beta_{ki}^{b}\right]$. It is noteworthy that applying the second-order algorithm significantly reduces the possibility of the vacancy returning to the previous site, $p_{i=j}^{(2)}$, in comparison to the first-order possibility $p_{i=j}^{(1)}$. Moreover, the average timestep in the second-order algorithm, $\Delta\vec{t}^{(2)}$, is substantially greater than its first-order counterpart $\Delta\vec{t}^{(1)}$. It suggests that the second-order algorithm bypasses flicker events stochastically by reducing backtracking and generating a larger timestep, thereby significantly enhancing the efficiency of the kMC algorithms

Here, all kMC simulations were performed using the second-order algorithm in a supercell with 30 × 30 × 30 FCC unit cells (108000 lattice sites) with a lattice constant of 4.046 Å. The side length of the supercells is 12.138 nm. There are 3090 Mg atoms, 2573 Zn atoms, and 1 vacancy in the supercells at a composition of Al-2.86 at.%Mg-2.38 at.%Zn-0.001 at.%vacancy. The solute concentrations are within the range of compositions of the 7075 Al alloys. The initial configurations were randomly distributed representing the solid solution at high temperatures. Hence, before kMC simulations, the configurations were annealed at 800 K (a typical solutionizing temperature for Al alloys) using the Canonical Monte Carlo (CMC) method for ~10^9 simulation steps. For the system of 30 × 30 × 30 FCC unit cells, the total energy usually converges within 10^7 simulation steps at 800 K. After this convergence, the average fluctuation of the total energy of the system with respect to the simulation step is approximately $\sim 1.9 \times 10^{-5}$ eV/atom.

2.3. CNT for Mg-Zn-based clusters

The steady-state nucleation rate of precipitation in the solid state is generally defined by the equation [69–75]:

$$J^{st} = Z\beta^* \exp\left(-\frac{\Delta G^*}{k_B T}\right) \tag{5}$$

where Z is the Zeldovich factor, ΔG^* is the nucleation barrier at the saddle points that depends on the free energy difference of solute atoms between the matrix and the precipitate phases, β^* is the rate at which a critical nucleus grows, which depends on the diffusivity of solutes that is the rate-determining species of precipitation. See Supplementary Note 3 for details to quantify the value of β^* and Z of a two-element nucleating phase [76,77].

To obtain the value of ΔG^*, we estimated the cluster formation free energy profile ΔG as a function of the number of Mg atoms, n_{Mg}, and Zn atoms, n_{Zn} at different temperatures by

$$\Delta G\left(n_{Mg}, n_{Zn}\right) = \Delta H\left(n_{Mg}, n_{Zn}\right) - T\Delta S\left(n_{Mg}, n_{Zn}\right) \tag{6}$$

where ΔH and ΔS are the cluster formation enthalpy and entropy, respectively.

For the calculation of ΔH, we ignore the effects of temperatures and external pressure to obtain the minimum energy of a solute cluster ($\Delta H \approx \Delta E$) based on the Monte Carlo simulations. Here, we applied the simulated annealing heuristic [78] (an adaptation from the Metropolis-Hasting algorithm [79]) to search for the optimal structural and formation enthalpy of solute clusters, ΔH. Although DFT calculations can provide a good energetic estimation of clusters and GP zones in Al–Mg–Zn alloys, it is difficult to get the most stable structures of clusters with the given n_{Mg} and n_{Zn}, because the possible configurations of solute clusters explode with an increase of n_{Mg} and n_{Zn}. The simulated annealing heuristic is performed with a decreasing temperature as the simulation step proceeds to find the global minimum configuration at 0 K. We chose a simulation supercell with a size of

$10 \times 10 \times 10$ FCC Al unit cell, with 4000 atoms in total. n_{Mg} Mg and n_{Zn} Zn solute atoms were placed randomly in the supercell. Each solute atom was set far from one another by at least a third nearest neighbor distance, 5.3 Å, which is the cutoff distance of our surrogate model for solute cluster energetics described in Section 2.1. In this way, we can estimate the enthalpy of the final solute clusters without calculation of any energetic contributions of the initial solid solution state. We ran $51 \times 86 = 4386$ simulated annealing calculations in total with different numbers of solute atoms involved (n_{Mg} from 0 to 50 and n_{Zn} from 0 to 85). For each simulated annealing calculation, the initial temperature was chosen as 800 K, and the cooling rate is $10^{-7} K$/step until the temperature reaches 0 K.

For the calculation of ΔS, as a simple approximation, we only consider the configurational entropy contributions when solute atoms from dilute solid solutions to form a single cluster. The formation entropy as a function of n_{Mg} and n_{Zn} is:

$$\Delta S\left(n_{\mathrm{Mg}}, n_{\mathrm{Zn}}\right) \approx k_B\left[n_{\mathrm{Mg}} \ln\left(x_{\mathrm{Mg}}\right) + n_{\mathrm{Zn}} \ln\left(x_{\mathrm{Zn}}\right)\right] \tag{7}$$

where x_{Mg} and x_{Zn} are the atomic concentrations of Mg and Zn in the model alloy.

2.4. CMC algorithms

The CMC algorithms are based on Monte Carlo methods that enable the exploration of equilibrium properties of a Canonical ensemble (fixed numbers and types of atoms at a constant temperature). CMC simulations apply canonical ensembles, which quantify the system's equilibrium behavior under controlled conditions of fixed temperature, a set volume of the simulation supercell, and a specific number of each type (chemical element) of occupants within the simulation system. The CMC simulations adopt the standard Metropolis–Hastings algorithm [79]. The probabilities of observing a state σ_i with energy $E(\sigma_i)$ in a system follows the Boltzmann distribution, which can be expressed as $P(\sigma_i) \propto \exp(-E(\sigma_j)/k_B T)$. Here $E(\sigma)$ represents the total energy Hamiltonian of the system which can be described by the surrogate model. This allows for the determination of the probability of a state σ_i with the total energy $E(\sigma_i)$ existing in the system. In the algorithm, a new state is proposed by swapping the position of a pair of atoms. The candidate pairs are chosen randomly with equal probability. However, for the simulation efficiency, the swaps between the same type of atoms are omitted since this type of swap does not result in any configurational or energetic evolution. When the new state σ_j with the total energy $E(\sigma_j)$ is proposed, the energy difference between the two states, $\Delta E = E(\sigma_j) - E(\sigma_i)$, is used to determine the probability of accepting the new state compared to the old one, $P_{ij} = \exp\left(-\frac{\Delta E}{k_B T}\right)$, where the value of P_{ij} ranges from 0 to ∞. If $P_{ij} \geq 1$ (i.e. $\Delta E \leq 0$, this attempt would decrease the total energy of the system), σ_j would be accepted. If $P_{ij} < 1$ (i.e. $\Delta E > 0$), σ_j would be accepted with probability P_{ij}. A uniformly distributed random number ξ between 0 and 1 is generated and compared with P_{ij}. The new state σ_j is accepted when $\xi \leq P_{ij}$. This algorithm enables the probability of an increase in the total energy, which ensures that the system is not trapped in a local minimum. As the temperature increases, there is a higher likelihood of the system having higher energy.

2.5. Revised kMC algorithm to simulate quenching processes

In all of the kMC simulations performed at constant temperatures, we utilized the initial configurations that were annealed at 800 K using CMC methods. Nevertheless, starting from the very first step, we apply the vacancy diffusivity at lower temperature conditions onto the state generated at higher temperatures (800 K). This always indicates that the simulations start with an infinitely fast cooling rate dropping from 800 K. Thus, the simulation at a constant temperature, especially that performed at 300 K using the 800 K equilibrium state as the initial configuration, might not accurately represent the precipitation kinetics that occur during quenching. Hence, by revising the kMC algorithm to update the temperature at each step, we can more closely mimic the actual temperature change during quenching, thus enhancing the accuracy of solute clustering of the simulation.

To implement the revised kMC algorithm, we first need to simulate the temperature curve for quenching using the finite element analysis method in the COMSOL Multiphysics simulation software [56]. In the simulation, we considered Al–Mg–Zn alloy samples in the form of wafers with a radius of 0.1 m and varying thicknesses ranging from 0.1 μm to 0.5 μm. These samples were then subjected to quenching within a cylindrical water tank, which has a radius of 0.5 m and a height of 0.5 m. The initial temperature of the alloy sample is set to 800 K. Simultaneously, the initial temperature of the water tank is at 300 K (room temperature). During the water quenching process, the primary heat transfer mechanism taken into account is convective cooling occurring at the interface between the alloy and the water. Although heat conduction and radiation also play a role in the overall heat transfer process, their effects are less significant relative to convection. To simplify the simulation and reduce the computational complexity, thermal insulation boundary conditions are applied to the external surfaces of the water tank, which assumes that no heat is exchanged between the water tank and the surrounding environment. This is less important for the temperature change of the alloy during the rapid quenching process.

After computing these temperature profiles, we integrated them into the revised kMC simulations to more accurately quantify the quenching process compared with kMC simulations at constant temperatures. The key difference lies in the temperature update at each step. The temperature is updated based on the temperature evolution profile $T(t)$ shown in Fig. 1(d) and the current simulation time t, using the equation $T_{n+1} = T(t_n + \Delta t)$. In this equation, T_{n+1} represents the temperature at the next step (step $n+1$), and t_n denotes the time at the current step (step n). Δt is the incremental time obtained from Eq. (4) applied at the current temperature T_n. In the original kMC algorithm [65,80–82], one of the underlying assumptions is that the simulation is conducted at a constant temperature throughout the simulation process. However, the revised kMC simulations would remain valid as long as the temperature remains nearly constant for numerous consecutive kMC steps (the number of steps comparable to the number of lattice sites in the supercell). This quasi-constant temperature criterion suggests that the temperature changes are gradual and do not significantly impact the overall simulation process. As long as this quasi-constant temperature condition is satisfied, we can confidently utilize the revised kMC algorithm to simulate quenching processes with greater accuracy and reliability. In all of the revised kMC simulations conducted for this study, at least $\sim 10^4$ to $\sim 10^7$ simulation steps are required to make a one-degree Kelvin change in the simulation temperature (details in Fig. 10 and the related discussions). These values are substantially large when compared to the number of atoms present in the supercell, which is 1.08×10^5. Consequently, the quasi-constant temperature criterion is adhered to, ensuring that the revised kMC algorithm remains a reliable approach for simulating quenching processes in Al–Mg–Zn alloys.

3. Results

3.1. KMC simulations at constant temperatures

The time evolution of the average energy per atom E of the whole simulation supercell for kMC simulations at different constant temperatures is shown in Fig. 3(a). E is expressed as $E = (E_{\mathrm{tot}} - E_{\mathrm{tot},0})/N_{\mathrm{tot}}$, where E_{tot} is the total energy of the system obtained from the aforementioned surrogate model and $E_{\mathrm{tot},0}$ denotes the total energy at the first frame that was generated by CMC simulations at 800 K. N_{tot} is the number of atoms in the supercell. For each curve, the initial zero energy corresponds to the solid solution state of the first frame. Initially, the

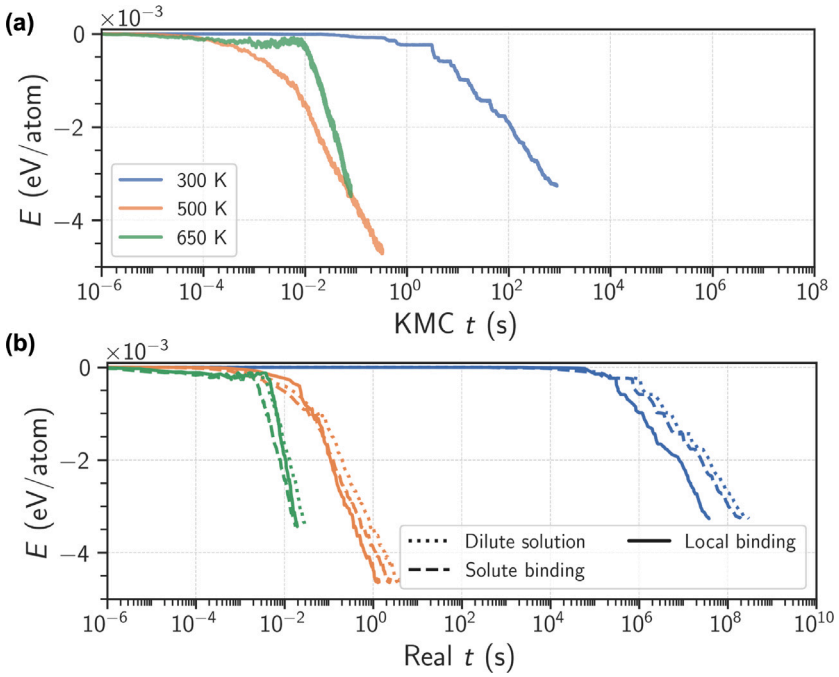

Fig. 3. Time evolution of the average energy per atom E of the whole supercell in the constant-temperature kMC simulations at 300 K (blue), 500 K (orange), and 650 K (green). (a): Evolution based on the stochastic time according to the original kMC algorithm. (b): The same evolution based on the scaled time using Eq. (8) due to the difference between the fixed vacancy concentration in the simulation supercell and the temperature-dependent equilibrium vacancy concentrations calculated from different approximations (dilute solution approximation, solute binding approximation, and local binding approximation [83–88]). In the figures that follow, only the stochastic time according to the original kMC algorithm is used. All kMC simulations in this study start from a random solid solution state obtained by CMC simulations at 800 K, whose energy is defined as the zero reference. (For interpretation of the references to color in this figure legend, the reader is referred to the web version of this article.)

values of E stay almost zero, indicating the system still stays in the solid-solution state without the nucleation of solute clusters. As the time increases to a critical point, the values of E start to drop, corresponding to the initiation of solute cluster nucleation and growth. This critical time for the energy drop can be regarded as the incubation time of solute nucleation, which is on the scale of 10^{-2}, 10^{-3}, and 10^{-1} second for the kMC simulations of 650 K, 500 K, and 300 K, respectively. Among these cases at different temperatures, the case of 500 K has the smallest incubation time because both the thermodynamic driving force for the solute clusters and the diffusivity of the vacancy are relatively high at intermediate temperatures. Too high or too low temperatures can result in a small thermodynamic driving force (due to entropic effects at high temperatures) or a vacancy diffusivity that is too low (due to large vacancy migration barriers at low temperatures), respectively. In addition, the energy changes of the whole kMC simulations supercell shown in Fig. 3(a), which start from the solid solutions obtained at 800 K as the zero-energy reference states, are at the scale of several meV per atom, which are typical values of thermodynamic driving forces for phase transformation in metallic alloys. These results suggest that our kMC simulations can present reasonable descriptions of solute clustering thermodynamics and kinetics in metallic alloys at constant temperatures with constant vacancy concentrations.

It is important to note that the value of the vacancy concentration used in kMC simulations remains constant and can be considerably greater than the vacancy concentration in the actual alloy during the aging process. In realistic cases, as the temperature drops, the vacancy concentration can decrease greatly due to its interactions with solute clusters, dislocations, and grain boundaries. The concentration varies the effective solute diffusivity and the expectation of a time step in the kMC simulations. In extreme cases, if the vacancy concentration is always equal to the value determined by thermodynamic equilibrium, the single-step time evolution can be scaled:

$$\Delta\bar{t}_{\text{scaled}} = \frac{c_{\text{vac}}^{\text{conf}}}{c_{\text{vac}}^{\text{local}}}\Delta\bar{t} \tag{8}$$

Here, $c_{\text{vac}}^{\text{conf}} = 10^{-5}$ denotes atomic vacancy concentration in the simulation supercell, $c_{\text{vac}}^{\text{local}}$ represents the local equilibrium vacancy concentration at different temperatures. The value of $c_{\text{vac}}^{\text{local}}$ can be determined by different estimations. The energy evolution profiles with the scaled time of the kMC simulations using Eq. (8) and different corrected $c_{\text{vac}}^{\text{local}}$ (from the dilute solution approximation, the solute binding approximation, and the local binding approximation) are shown in Fig. 3(b). See Supplementary Note 4 for details of different approximations [83–88]. For the kMC simulation at 300 K (represented by blue lines in both Fig. 3(a) and (b)), the time evolution curve exhibits different required time lengths for the energy drop in Fig. 3(a) and (b). This is attributed to the equilibrium vacancy concentration at 300 K being significantly lower than in the supercell, which leads to a considerable scaling in the energy–time curve. Nevertheless, we can still find that it takes at least a few seconds or a few days for a noticeable energy decrease to occur based on Fig. 3(a) and Fig. 3(b), respectively, no matter which scaled method is applied. For the kMC simulation at 500 K (indicated by orange lines), the time evolution curve in Fig. 3(b) displays a less pronounced scaling effect relative to its counterpart in Fig. 3(a) due to the higher equilibrium vacancy concentration at this temperature. Here, a significant energy decrease is rapidly observed due to the fast kinetics at higher temperatures, which takes about $10^{-2} \sim 10^{-1}$ seconds based on Fig. 3(a) and Fig. 3(b). In the kMC simulation at 650 K (represented by green lines), the energy–time curve is not significantly scaled since the equilibrium vacancy concentration at 650 K is close to that in the supercell. A rapid and significant energy decrease is also observed at 650 K, within approximately 10^{-2} seconds. The fast energy drops at both 650 K and 500 K suggest that the kinetics of solute clustering can be quite fast at higher temperatures, much less than 0.1 s according to Fig. 3(a) and (b).

Snapshots visualized by OVITO [89] of gathered solute atoms in supercells with the same value of E (-3×10^{-3} eV/atom) generated by kMC simulations at different temperatures are shown in Fig. 4(a)–(c) (Fig. 4(a) at 650 K, Fig. 4(b) at 500 K, and Fig. 4(c) at 300 K). For each configuration shown in the snapshots in Fig. 4, a solute cluster

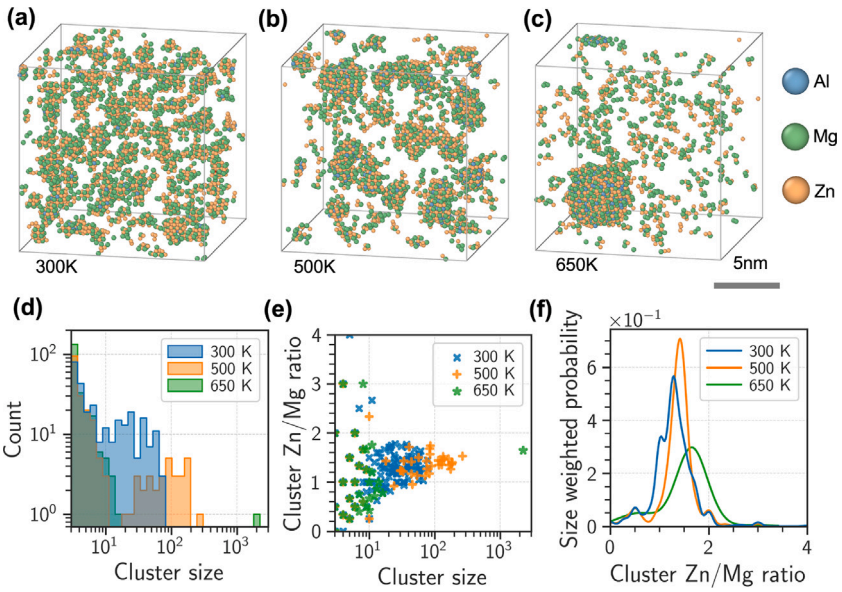

Fig. 4. Snapshots and analyses of the constant-temperature kMC simulations at 300 K, 500 K, and 650 K show the changes in solute cluster structural features. (a)–(c): Snapshots of solute clusters when the supercell average energy $E = -3 \times 10^{-3}$ eV/atom relative to the initial solid solution state in kMC simulations at 300 K (a), 500 K (b), and 650 K (c), respectively. Only clustered atoms (solute atoms (Mg (green) or Zn (orange)) that have at least 2 other solute atoms as their 1st nearest neighbors and their neighboring Al (blue) atoms that have more than 6 clustered solute atoms as their first nearest neighbors) are plotted and counted. These criteria for clustered atom identifications are also applied to all other figures. (d)–(f): Analyses of the kMC simulation snapshots at different temperatures. (d): Histograms of the cluster size defined by the number of clustered atoms based on the above cluster identification criteria. (e): Correlations between Zn/Mg ratio in clusters and the cluster sizes. (f): Kernel density estimations of the Zn/Mg ratio of atoms in clusters. (For interpretation of the references to color in this figure legend, the reader is referred to the web version of this article.)

has at least 3 solute atoms (Mg or Zn) that can be connected together by first-nearest neighbor bonds and also Al atoms that have more than 6 solute atoms (from the same cluster) as their first-nearest neighbors. The distributions of cluster size, which are quantified by the number of atoms belonging to this cluster, are shown in Fig. 4(d). For the kMC simulation at 300 K, numerous clusters exhibit sizes under 80 atoms, with diameters falling within 1 nm (by assuming the cluster is a sphere). The snapshot reveals that these clusters are evenly distributed throughout the entire supercell, suggesting a uniform nucleation behavior at this temperature. For kMC simulation at 500 K, larger clusters appear but the overall number of these clusters decreases relative to the low-temperature case (300 K). This suggests that a higher temperature may cause a shift in the cluster size distribution, yielding fewer but larger clusters. As the temperature of the simulation increases to 650 K, a distinctive shift in cluster distribution occurs. A single prominent cluster with a size exceeding 1000 atoms, and a diameter of ~ 4 nm, emerges while the rest of the clusters remain comparatively smaller, with sizes not exceeding 30 atoms for each cluster. With respect to small clusters such as atomic triplets and quartets, which are likely below the critical size of nuclei [3,4,90], increased temperatures enhance the kinetics for the diffusivity of solute atoms, resulting in more rapid and efficient Mg-Zn bonding, ultimately leading to an increased number of these sub-critical clusters.

Besides the sizes of clusters, the chemical concentration of solute clusters is also greatly affected by simulation temperature. The Zn/Mg ratios of the stable precipitates in 7XXX series Al alloys, such as the η phase $MgZn_2$, are typically around 2:1. But this ratio can vary depending on the specific composition, heat treatment, and aging time [33]. Fig. 4(e) shows the correlation between the size of clusters (X-axis) and the Zn/Mg ratio in clusters (Y-axis) at different simulation temperatures (blue cross signs for 300 K, orange plus signs for 500 K, and green stars for 650 K). Since there are many clusters with sizes smaller than 10 atoms in all simulations with different temperatures, these small clusters can exhibit a wide range of Zn/Mg ratios from 0 (Mg-only clusters) to infinity (Zn-only clusters). Thus, we need to pay more attention to the clusters with larger sizes, such as those with more than 10 atoms. From the simulations at 300 K to 500 K, we observe a trend in the Zn/Mg ratio of data points becoming more narrowed as the average size of the clusters increases. In Fig. 4(f), the kernel density estimations of the Zn/Mg ratio of clusters are presented, with the weight of the cluster size measured in its number of atoms. These estimations reflect all aggregated atoms on a smooth and continuous distribution of Zn/Mg ratios in the clusters. The peaks in the plot can be used to describe the most representative Zn/Mg ratio of solute clustering in the supercell. The peak values in the plot are 1.26, 1.43, and 1.63 for the kMC simulations at 300 K, 500 K, and 650 K, respectively. This shows that as the simulation temperature increases, the peak value, or the most representative Zn/Mg ratio, also increases.

The average Zn/Mg ratio for clusters with sizes greater than 10 atoms can also be used as another indicator to evaluate the chemical concentration of solute clusters. The evolution of the averaged Zn/Mg ratio in clusters with respect to time and energy change is shown in Fig. 5(a) and Fig. 5(b). For the simulation at 300 K in Fig. 5(a), the Zn/Mg ratio reaches around 1.4 at approximately 1 s (which is at the same scale as the incubation time we discussed in Fig. 3(a)). After this point, the Zn/Mg ratio undergoes a slight decrease, settling around 1.25 as the time t and energy E continue to evolve. This behavior suggests a thermodynamic driving force for the formation of clusters with a lower Zn/Mg ratio at room temperature. For the simulations at 500 K, the ratio almost remains constant at around 1.4. For the simulation at 650 K, there is a noticeable increase in Zn/Mg ratios to 1.8 after it reaches the incubation time (10^{-2}), suggesting that higher Zn/Mg ratio clusters are preferred at increased temperatures. As shown in Fig. 5(b), when the energy change (the value of E on the X-axis) is at the same value, we can still see the trend that clusters formed at higher simulation temperatures tend to have higher Zn/Mg ratios. For example, when the energy change is E =−1.5 eV/atom or more negative, the averaged Zn/Mg ratio stays ~1.6, ~1.4, and ~1.3 for simulations at 650 K, 500 K, and 300 K, respectively. These results indicate that there could be different internal structures of solute clusters formed at different temperatures due to thermodynamic factors, which will be discussed in the next section.

The time-dependent cluster distributions in terms of the cluster radius defined by the size (number of atoms) at different temperatures are investigated in Fig. 6(a)–(c), while the analysis of individual

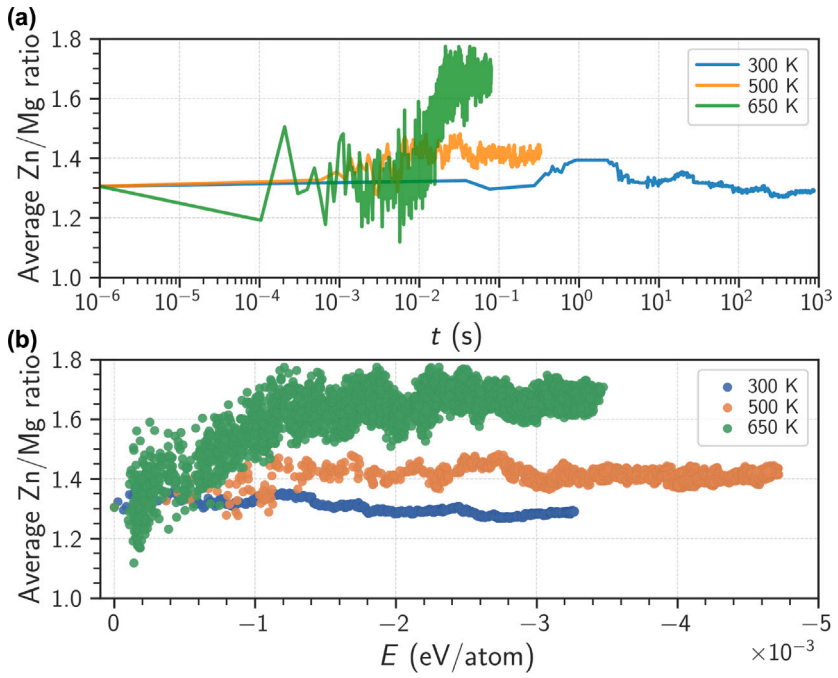

Fig. 5. Temperature effects on solute cluster compositions demonstrated by the evolution of the average Zn/Mg ratio for all clusters with a size larger than 10 clustered atoms (all clustered atoms defined by the criteria described in the caption of Fig. 4) in constant-temperature kMC simulations at 300 K (blue), 500 K (orange), and 650 K (green). (a): The average Zn/Mg ratio as a function of time. (b): The correlations between the average Zn/Mg ratios and the average energy per atom of the whole supercell using the initial solid solution state as the zero reference. (For interpretation of the references to color in this figure legend, the reader is referred to the web version of this article.)

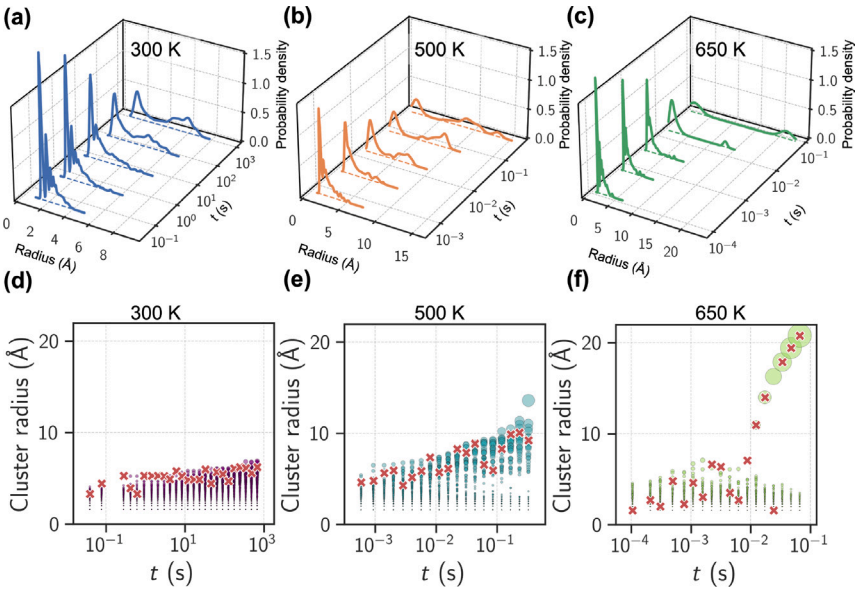

Fig. 6. Analyses for cluster size in terms of cluster radius in the kMC simulations at different temperatures. The cluster radius is calculated by assuming the solute cluster is a sphere. (a)–(c): Evolution of cluster radius at logarithmically selected time points during the simulations, shown as a cluster size-weighted probability distribution function. (e)–(h): Analyses for individual clusters across all time frames in the revised kMC simulations showing the correlations between the radius of clusters and simulation time. The color of the dots indicates the temperature (defined by the color bar at the bottom) at the corresponding simulation time. The size of the dots in the plots denotes the size of the clusters. Red crosses highlight the clusters that contain the vacancy at the corresponding simulation time. These subfigures share the same *Y*-axis ticks. (For interpretation of the references to color in this figure legend, the reader is referred to the web version of this article.)

clusters extracted from different time frames of the simulation results is presented in Fig. 6(e)–(h). The size of the dots in Fig. 6(e)–(h) represents the size of the corresponding cluster. Some of the clusters are highlighted by red crosses in the figures, meaning these clusters contain a vacancy at that time point. Fig. 6(a)–(c) shows the changes in cluster distribution by radius throughout simulations at constant temperatures. Here, the distributions of selected times are presented as a cluster size-weighted probability function, ranging from single solute atoms to the largest clusters found in each simulation. The distribution reflects how solute atoms aggregate to form clusters of varying sizes. At the beginning of the simulation at 300 K, we observe a small peak with a radius of approximately 5 Å emerge within 1 s in Fig. 6(a), signifying a low density of nuclei at the initial state. As the simulation progresses, the peak not only shifts to larger radii but also increases in magnitude, suggesting that the clusters are not only growing in size (shown in Fig. 6(d)) but also becoming more densely populated. At the

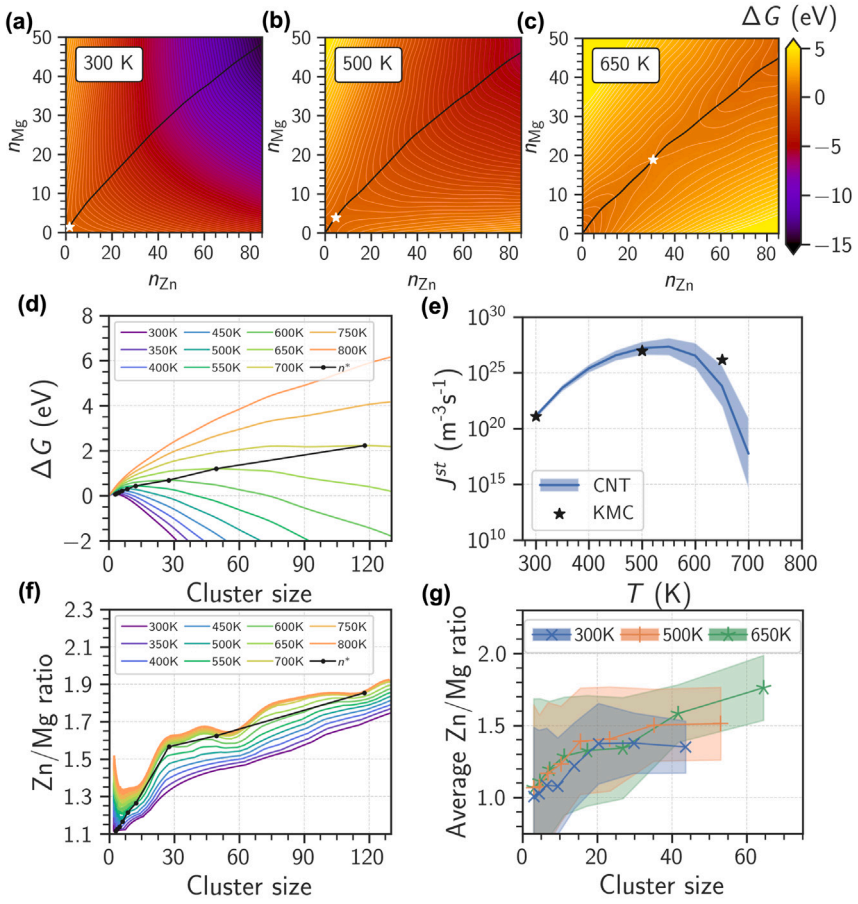

Fig. 7. Free energy contours and analyses of Mg–Zn-rich clusters. (a)–(c): Calculated cluster formation free energy, ΔG, of the alloy Al-2.86 at.%Mg-2.38 at.%Zn with respect to n_{Mg} and n_{Zn} ((the numbers of Mg and Zn atoms in the cluster) at 300 K (a), 500 K (b), and 650 K (c). In each of them, the black line indicates the minimum energy pathway and the white star marks the saddle point at the corresponding temperature. (d): ΔG along the minimum energy pathway in a range of temperatures from 300 K to 800 K. The black line connects the cluster at the critical size (saddle point) at different temperatures. (e): The steady-state nucleation rate, J^{st}, of Mg–Zn-rich clusters obtained from the constant-temperature kMC results (black stars) and calculated from the CNT model (blue lines) using Eq. (5). The blue shaded error bar shows the confidence bounds based on the ±10% of the ΔG^*. (f): The change of Zn/Mg ratio along the minimum energy pathway in a range of temperatures from 300 K to 800 K. The black line connects the cluster at the critical size (saddle point). (g) The averaged Zn/Mg ratio for clusters of different sizes during the steady nucleation stage from the constant-temperature kMC simulations. The shaded regions indicate the standard deviations. (For interpretation of the references to color in this figure legend, the reader is referred to the web version of this article.)

end of the simulation, around 1000 s, the maximum size of clusters reaches ~7 Å in radius. As shown in the final distribution curve, about half of the solute atoms have coalesced into clusters with radii in the range of approximately 5-6 Å. Similar trends can be observed in the simulations of 500 K and 650 K. In the simulation of 500 K, the initial peaks of Fig. 6(b) are broader and located at larger radii compared to the 300 K simulation, implying that the clusters start larger at this temperature. As time advances, these peaks also move towards larger radii and increase in height. However, the clusters here reach even greater sizes; by the end of the simulation, a significant concentration of solute atoms is found in clusters with radii greater than 12 Å. At an even higher temperature of 650 K, the clustering phenomenon is fast. Within 0.1 s, about one-half of the solute atoms have merged into the single, largest cluster as shown in Fig. 6(c). The remainder of the solute atoms exist as smaller and less stable nuclei. We can see from Fig. 6(f) that many smaller clusters are consumed for the growth of the largest cluster. From the red crosses denoted in Fig. 6(d)–(f), we observe that the vacancy jumps among those larger clusters in the simulation at 300 K. In the simulations of 500 K and 650 K, vacancy shows higher mobility caused by the higher temperature.

3.2. CNT model

The results from our CNT model also confirm the differences in Mg–Zn-rich clusters of size, density, and compositions during the nucleation stage. Conventionally, the nucleation barriers of clusters are attributed to the contributions from the volumetric and interfacial free energies. However, for small clusters with only a few atoms, it is difficult to distinguish the volumetric and interfacial contributions. Hence, we adopted a method that evaluates ΔG by considering both enthalpic and entropic factors as Eq. (6) [4,90–94]. As described in Section 2.3, due to the structural complexity of multi-component clusters and GP zones in Al–Mg–Zn alloys [34,95,96], it is difficult to directly estimate the stable structures of the cluster composed of specific numbers of n_{Mg} and n_{Zn}. Therefore, we employed a Monte Carlo-based simulated annealing heuristic to search for the most stable structures of clusters and corresponding ΔH, while the ΔS is quantified by Eq. (7).

The free energy landscape maps at 300 K, 500 K, and 650 K are presented in Fig. 7(a)–(c), respectively. Contour maps at more temperatures can be found in Supplementary Note 5. These maps are constructed based on n_{Mg} and n_{Zn} within clusters. The black lines in each plot trace the minimum free energy pathways, which signify the most energetically favorable routes for cluster growth at these temperatures when the diffusivity of solute atoms is sufficient. The white star marks the critical cluster which is at the saddle point ($n_{Mg} = n^*_{Mg}$ and $n_{Zn} = n^*_{Zn}$) of the free energy profile. This critical point is mathematically characterized by the conditions where the first derivatives of ΔG with respect to n_{Mg} and n_{Zn} are zero: $\frac{\partial \Delta G}{\partial n_{Mg}} = 0$ and $\frac{\partial \Delta G}{\partial n_{Zn}} = 0$. Fig. 7(d) illustrates the free energy change along these

minimum energy pathways from 300 K to 800 K. In this plot, the black line interconnects the critical cluster at different temperatures, highlighting the significant temperature dependency of the critical cluster. At the lower temperature of 300 K, the critical cluster size, n^*, is approximately 3 atoms, with a critical free energy barrier, ΔG^* of about 0.07 eV. As the temperature rises, there is a notable increase in both the critical cluster size and the energy barrier. Specifically, at 500 K, the critical size n^* escalates to 9 atoms, and the energy barrier G^* climbs to 0.30 eV. Further, at 650 K, n^* reaches 49 atoms, and ΔG^* is about at 1.19 eV. It is notable that both the n^* and ΔG^* start to increase rapidly when the temperature goes beyond 650 K (Supplementary Note 6), which indicates that it is thermodynamically difficult to form stable clusters at these elevated temperatures.

The investigation into the nucleation rate, J^{st}, and the chemical composition of clusters during the steady-state nucleation stage was conducted using both the CNT model and kMC simulations. J^{st} is calculated at different temperatures and plotted in Fig. 7(e). The estimations of J^{st} from the kMC simulations at the corresponding constant temperatures are also marked in Fig. 7(e). J^{st}, as computed by Eq. (5) reaches its peak within the temperature range of approximately 500 to 600 K, which is in agreement with the results from the kMC simulations, as depicted in Fig. 7(e). Furthermore, Fig. 7(f) presents an analysis of the Zn/Mg ratio relating to cluster size along the minimum free energy pathway across a spectrum of temperatures. As indicated by this figure, both cluster size and temperature would affect the Zn/Mg ratio. Clusters of the same size exhibit a higher Zn/Mg ratio at increased temperatures. Similarly, at the same temperature, the Zn/Mg ratio increases with cluster size. These results explain the composition differences of clusters observed in the kMC simulations, where clusters formed at higher temperatures tend to be larger compared to those formed at low temperatures. They exhibit a higher Zn/Mg ratio due to the combined effects of size and temperature. Additionally, the Zn/Mg ratio of clusters during the steady-state nucleation state was analyzed through kMC simulation results, as shown in Fig. 7(g). Here, smaller, low-temperature clusters possess a lower Zn/Mg ratio, aligning with the results calculated from the CNT model as in Fig. 7(f).

3.3. CMC simulations at constant temperatures

To further investigate the chemical concentration and the short-range ordering of clusters at different temperatures at the equilibrium states after the nucleation stage, we set up a series of CMC simulations across a temperature spectrum, with decrements of 5 K from 800 K to 275 K, utilizing the identical supercell configuration as in the kMC simulations. We choose to use CMC simulations as supplementary to take advantage of both the CMC and the kMC methods. While kMC simulations enable the time evolution study of the system, CMC simulations can provide a more thorough revealing of (meta)-stable states at (quasi-)equilibrium that cannot be easily accessed by kMC simulations. The choice of temperature range was motivated by the desire to capture both the low-temperature domain, where cluster formation is largely driven by thermodynamics, and the high-temperature domain, where high entropy effects prevent the clustering of solutes. To ensure the accuracy and reliability of our CMC simulations, and to lessen the likelihood that the system gets trapped in a local minimum, we utilize the final configuration from a higher temperature as the starting point for the subsequent lower temperature simulations. At each temperature, we carried out 10^9 CMC simulation steps to achieve (quasi-)equilibrium of the system. This number is sufficient relative to the total lattice sites of 1.08×10^5 in the supercell. Typically, CMC simulations of the system converge within 10^8 steps.

During the CMC simulations, we analyzed the evolution of converged E at different temperatures T and plotted the results in Fig. 8(a). The total energy E remains almost constant and close to zero when the temperature is above 700 K. At these high temperatures, the increased atomic mobility effectively cancels out solute-solute interactions, and only atomic pairs and small clusters exist within the supercell. However, as the temperature drops below 700 K, the thermodynamic driving forces of solute clustering begin to dominate, and E decreases significantly as a large cluster forms. As the temperature continues to decrease, E keeps dropping with the size of the formed cluster increasing. It is notable that there is a change in the slope of the E - T curve at approximately 400 K. This change may signify a possible structural transition or phase change of the cluster.

Besides the energetic information, we conducted additional analyses including the chemical concentration of solute clusters for the CMC simulations. At each temperature, 100 configurations sampled from the last 10^8 steps are uniformly selected. The results are plotted as Fig. 8 (b)–(d), where the lines with shaded error bars are the averaged results of data at the same temperature. The evolution of the Zn/Mg and (Al+Zn)/Mg ratios in all relatively large solute clusters (each cluster has at least 10 atoms) at various temperatures are displayed in Fig. 8(b), the fractions of elements (Al, Mg, or Zn) in aggregated clusters are shown in Fig. 8(b), and the evolution of Mg and Zn atoms remaining in the Al matrix are shown in Fig. 8(c). When the temperature is above 700 K, only a small amount of Mg and Zn atoms are aggregated in clusters of at least 10 atoms. Almost no Al atom can be found in the clusters. The Zn/Mg ratio in the clusters is around 1.25 with a large fluctuation, while the ratio in the whole alloy is roughly 0.83. This observation indicates that even small Mg-Zn clusters tend to have more Zn atoms compared to Mg atoms [39,40], which is also close to the value estimated from the CNT model for small clusters of 1.3 (Fig. 7(f)). As the temperature is reduced below 700 K, the large clusters start to appear as denoted by a significant energy drop (Fig. 8(a)) due to the formed Mg-Zn bonds. The Zn/Mg ratio quickly increases as shown in Fig. 8(b). This increase in the Zn/Mg ratio is accompanied by the incorporation of more Zn atoms than Mg atoms into large clusters as indicated by the drops of solute remaining in the Al matrix shown in Fig. 8(d). At the same time, a great amount of Al atoms also goes into the formed clusters as shown by the Al curve from Fig. 8(c). As the temperature continues to drop from 700 K to ~ 400 K, although the fractions of both Mg and Zn atoms in the matrix in Fig. 8(d) keep decreasing as the clusters grow, the average Zn/Mg and (Al+Zn)/Mg ratios in all clusters drop smoothly with decreasing temperature as shown in Fig. 8(b). In this stage, more Mg atoms go into the cluster compared with Zn or Al (Fig. 8(c)). This trend continues until the temperature drops below 400 K. At this point, almost all of the available Zn atoms have been aggregated into solute clusters as indicated by Fig. 8(c), and the Zn atoms within the matrix are nearly consumed. Starting from here, as the temperature keeps decreasing, more Mg atoms join the cluster, leading to a sudden transition of the slope of the Zn/Mg ratio curve at ~400 K as indicated by Fig. 8(b), also corresponding to a possible structural transition of the cluster. It is also notable that as the temperature drops, the fraction of Al in the cluster keeps dropping as shown in Fig. 8(c), which is also suggested by Fig. 8(b) where the (Al+Zn)/Mg ratio changes faster compared to the Zn/Mg ratio.

To further validate our findings, we examined the internal structures of the clusters produced from CMC simulations at two different temperatures: 650 K and 300 K. As depicted in Fig. 9, these clusters were sliced along {100} planes for analyses alongside the atomic structures in unit cells extracted from the cluster. The high-temperature cluster exhibits translational symmetry along the ⟨001⟩ direction, consisting of two layers as shown in Fig. 9(a): the first layer is made up almost entirely of Zn atoms, while the second layer consists of a combination of both Mg and Zn atoms. As the temperature is relatively high, there are a great number of substitutional Al atoms in the cluster on the Zn sites. This type of structure closely resembles the $L1_2$ structure, illustrated in Fig. 9(b). Alternatively, the low-temperature cluster in Fig. 9(c) also exhibits translational symmetry along the ⟨001⟩ direction,

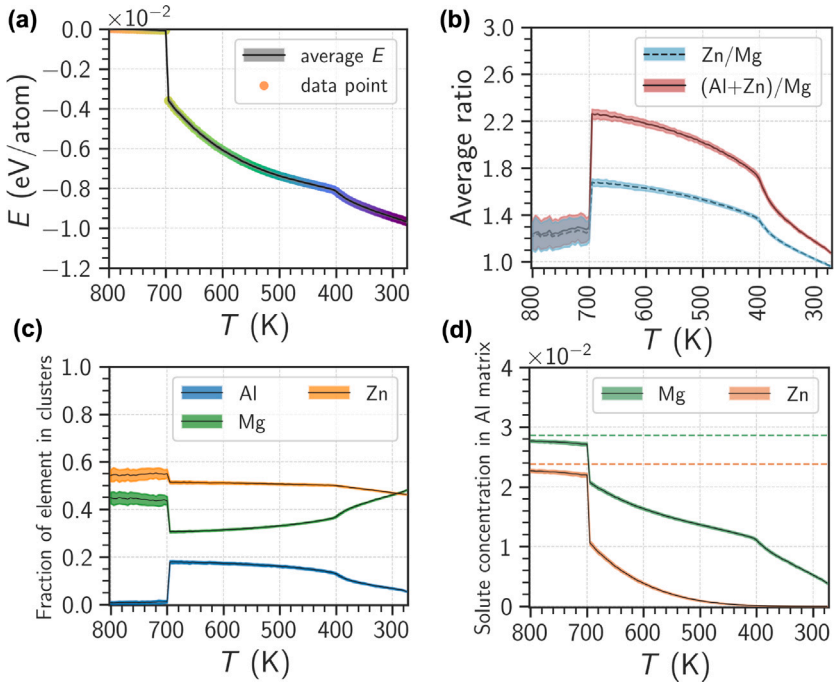

Fig. 8. Canonical Monte Carlo (CMC) simulation results as functions of the CMC simulation temperature show thermodynamic properties of solute clusters in the same kMC simulation supercell. (a): Evolution of the energy per atom E of the whole CMC simulation relative to the initial solid solution state. (b): Evolution of the average Zn/Mg ratio and (Al+Zn)/Mg ratio in all clusters with a size larger than 10 clustered atoms. (c): Evolution of fractions of Al, Mg, or Zn in all clusters with a size larger than 10 clustered atoms. (d) Evolution of the concentrations of solute atoms (Mg or Zn) remaining in the Al matrix. The dashed lines represent the overall concentration of each solute in the alloy.

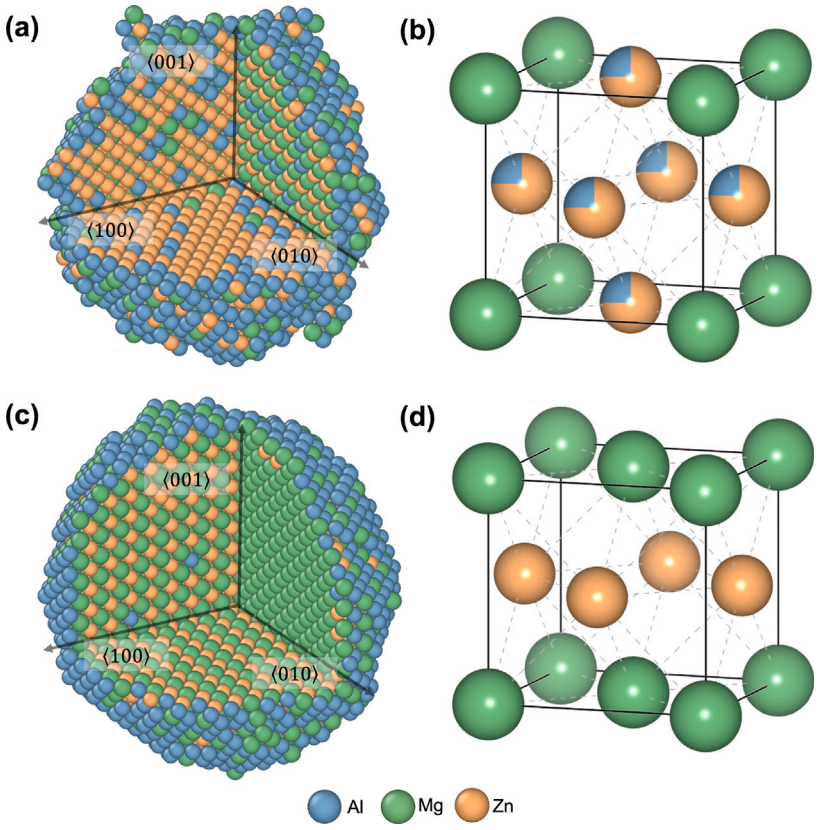

Fig. 9. Solute cluster phase transformation demonstrated by atomistic structures of clusters generated from CMC simulations at 650 K and 300 K. (a): A high-temperature cluster shows two alternative layers of atomistic structures along ⟨001⟩: one layer of mainly Zn and Al atoms; another layer of a mixture of mainly Mg and Zn/Al atoms. This structure is similar to the $L1_2$ structure shown in (b), where Mg atoms mainly occupy the corner sites and Zn/Al atoms mainly occupy the face center sites. (c)–(d): A low-temperature cluster also shows two alternative layers of atomistic structures along ⟨001⟩: one layer of mainly Zn and another layer of mainly Mg. This structure is close to the $L1_0$ structure shown in (d).

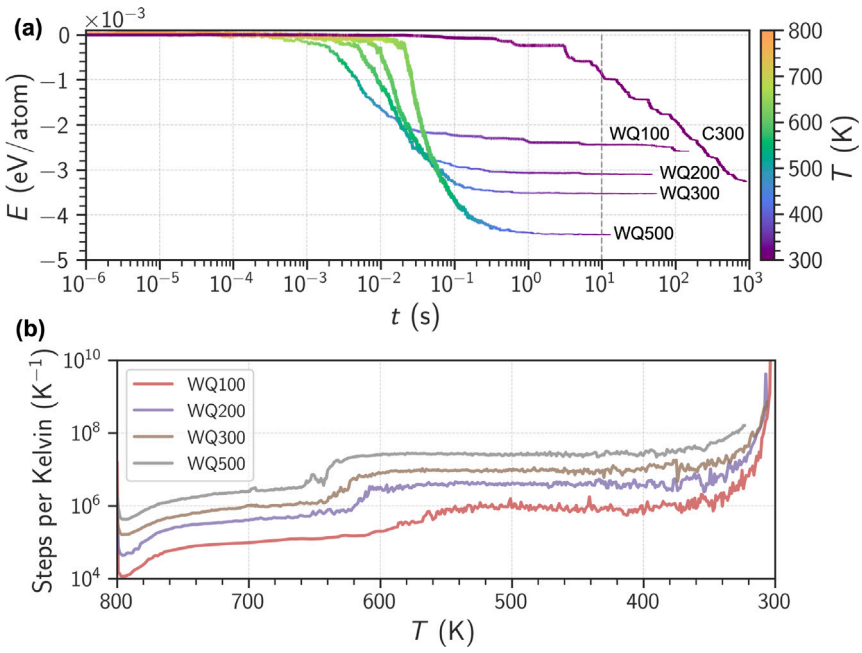

Fig. 10. Results of the normal (constant-temperature) and revised kMC simulations of the quenching processes following different temperature evolution profiles. Here, C300 means the constant-temperature kMC simulations at 300 K as plotted in Fig. 3(a). WQ100, WQ200, WQ300, and WQ500 correspond to different temperature evolution profiles shown in Fig. 1(d). (a): Time evolution of the average energy per atom E of the simulation supercell relative to the initial solid solution state. In each evolution curve, the time evolution of the simulation temperature is denoted by the colors defined in the right color bar. (b): The number of kMC simulation steps required to change the simulation temperature by one-degree Kelvin as a function of the simulation temperature during water quenching (WQ), indicating the revised kMC simulations can be approximated as the normal constant-temperature kMC simulations in a large number ($10^4 \sim 10^7$) of simulation steps.

featuring two layers. In this instance, one layer is comprised exclusively of Zn atoms, while the other layer contains only Mg atoms. There are fewer point substitutions due to the lower temperature. This type of structure features the $L1_0$ structure of MgZn as displayed in Fig. 9(d). The transition from the $L1_2$-like to $L1_0$-like structures explains the aforementioned change of chemical concentration. For the high-temperature $L1_2$ structure of $MgZn_3$, the Zn/Mg ratio for the cluster of perfect bulk compounds is 3:1 (in reality, the Zn/Mg ratio is always less than 2 because of the substitutional Al atoms and some anti-site occupations illustrated in Fig. 9(a)). However, for the low-temperature $L1_0$ structure, the Zn/Mg ratio is 1:1. This difference can explain the trend in the Zn/Mg ratio in kMC simulations at different temperatures as shown in Fig. 5, where the high Zn/Mg ratio at high-temperature kMC simulations is driven by the thermodynamic effects revealed by our CMC simulations.

3.4. Revised kMC simulations with different cooling rates

As mentioned in Section 2.2, the initial configurations were annealed at 800 K using the CMC method for the kMC simulations at constant temperatures. However, this always implies that the simulations start with an infinite cooling rate from 800 K, which may not reflect what really happens during a quenching process. Thus, we applied the revised kMC simulation algorithm as described in Section 2.5 to study solute clustering with the different cooling temperature profiles plotted in Fig. 1(d).

Fig. 10(a) displays the time evolution of the average energy per atom E of the whole simulation supercell with different cooling temperature profiles. The energy–time curve 'WQ100' represents the energy change with the cooling rate of an Al alloy sample with a thickness of 100 μm that has undergone water quenching. Similarly, other 'WQ' curves are from the sample with a thickness in μm of the number following 'WQ', while the 'C300' curve denotes the kMC simulation at a constant 300 K temperature, which can be viewed as an infinite cooling rate because it is a sudden change from the 800 K equilibrium to 300 K. It is notable that during such rapid quenching processes of WQ and C300 simulations, vacancy concentrations would be far from the equilibrium states and remain almost unchanged until several minutes after quenching according to a recent study [83]. Hence, in the WQ and C300 simulations, the time correction is not necessary since our initial vacancy concentration is close to the 800 K equilibrium. As shown in Fig. 10(a), significant energy drops are observed when the temperature reaches around ~ 650 to ~ 620 K for all WQ cases. Although our CMC simulation results in Fig. 8(a) suggest that solute clustering may occur at 690 K, an overcooling of several tens of Kelvin is necessary for nucleation of solute clustering under such rapid cooling conditions. It requires a longer time to reach this point as the thickness of the samples increases (~ 2×10^{-3} seconds for WQ100, ~ 5×10^{-3} seconds for WQ200, ~ 1×10^{-2} seconds for WQ300 and ~ 2×10^{-2} seconds for WQ500) because the cooling rate gets slower. This phenomenon is also supported by Fig. 10(b), which shows the simulation steps required to make a one-degree Kelvin change in simulation temperature. As discussed in Section 2.5, Fig. 10(b) demonstrates that it always requires $10^4 \sim 10^7$ kMC simulation steps to make a one-degree Kelvin change in simulation temperature for all WQ cases, so these quasi-constant temperature conditions make the revised kMC algorithm a reliable approach for simulating quenching processes in Al–Mg–Zn alloys. At the temperature where E greatly drops, the simulation steps required are also remarkably increased around ~ 650 to ~ 620 K. It is because more low-barrier vacancy migration events would happen at these temperatures during the simulation as the cluster forms. These clusters create local lattice distortions as well as lower-barrier MEPs. As a result, the transition rates r_i increase, and average simulation timesteps decrease greatly according to Eq. (2) and Eq. (4). After that, the energy curves in Fig. 10(a) exhibit a steep decline, suggesting more cluster nucleation and the growth of clusters driven by vacancy diffusion over time and an increased thermodynamic driving force due to decreasing temperature.

When the temperature falls below 400 K, the energy evolution of all WQ cases in Fig. 10(a) is almost frozen, where the diffusion of the vacancy is considerably suppressed and the vacancy gets trapped within large solute clusters (detailed analyses of vacancy trapping

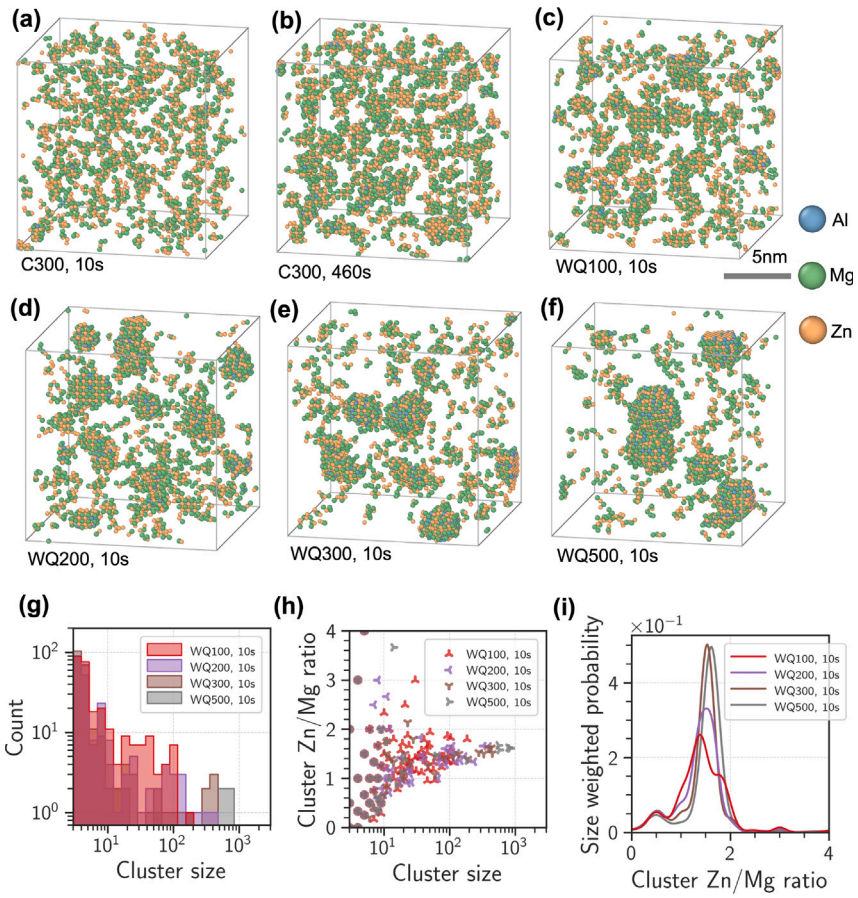

Fig. 11. Snapshots and analyses of the normal and revised kMC simulation results with different temperature evolution profiles defined in Fig. 1(b): C300 (infinite fast cooling from 800 K to 300 K), WQ100, WQ200, WQ300, and WQ500. (a)–(f): Snapshots of revised kMC simulation results showing solute clustering in cases of C300 at t = 10 s (a), C300 at t = 460 s (b), WQ100 at t = 10 s (c), WQ200 at t = 10 s (d), WQ300 at t = 10 s (e) and WQ500 at t = 10 s (f). (g)–(i): Analyses of the revised kMC simulation results at specific time snapshots defined in (c)–(f). (g): Histograms of the cluster size, which is defined by the number of clustered atoms according to explanations in the caption of Fig. 4. (h): Correlations between Zn/Mg ratio in clusters and cluster sizes. (i): Kernel density estimations of Zn/Mg ratio of clustered solute atoms in all clusters.

are described in Figs. 13 and 14 and the corresponding discussions). This occurs because these solute clusters grow rapidly and become more ordered at medium temperatures, creating huge basins in the energy profile. With the temperature dropping, the system becomes less capable of overcoming the energy barriers of these energy basins, and the energy curves are converged as shown for all the WQ cases in Fig. 10(a). Since the medium temperatures (~ 500 K) are more suitable for cluster nucleation and growth suggested by kMC simulations at constant temperatures (Section 3.1), the WQ simulations with lower cooling rate and more time near 500 K tend to reach a lower E plateau. The WQ500 simulation reaches the lowest ~−4.4 meV per atom when its energy curve converges compared to ~−2.5 meV for WQ100, ~−3.1 meV for WQ200, and ~−3.5 meV for the WQ300 case. However, for the C300 case, the kinetics (vacancy diffusivity) becomes significantly hindered due to the low temperature, while the initial thermodynamic driving force (overcooling) is larger than in the WQ cases. Thus, it takes about 10^{-1} seconds until a drop of E can be observed. In the case of C300, the energy keeps dropping without showing any convergence similar to the WQ cases. This is a result of the temperature remaining constant and all the clusters are nucleated and formed at the same temperature, and all of these clusters from C300 have small sizes as shown in Fig. 4(a) and the following Fig. 11(a) and (b). Hence, there is no significant vacancy trapping effect of these clusters compared to larger clusters from the WQ cases.

Snapshots of aggregated solute atoms generated by revised kMC simulations with different cooling rates are shown in Fig. 11(a)–(f) (Fig. 11(a) of C300 at t = 10 s, Fig. 11(b) of C300 at t = 460 s, Fig. 11(c) of WQ100 at t = 10 s, Fig. 11(d) of WQ200 at t = 10 s, Fig. 11(e) of WQ300 at t = 10 s, and Fig. 11(f) of WQ500 at t = 10 s). We applied the same criteria to identify clusters as we did for Fig. 4. The distributions of the size of clusters are shown in Fig. 11(g). For the WQ100 case, clusters with sizes around 100 atoms can be observed. In the WQ200 case, the supercell contains an abundance of clusters that exceed 200 atoms, with the largest cluster comprising up to 400 atoms. For the WQ300 case, several clusters with more than 400 atoms exist, and in the WQ500 case, the largest cluster identified contains approximately 800 atoms. In addition, the overall number of clusters continues to decrease in this case. This observed trend of cluster size distributions with decreasing cooling rate shows similarities to the trend of cluster size distribution changes in the constant-temperature kMC simulation cases with an increasing simulation temperature changing from 300 K to 500 K, as shown in Fig. 4(d). This correlation occurs due to the rapid growth of solute clusters at medium temperatures, approximately around 500 ~ 600 K. When the cooling rate is slower, the material spends more time at these medium temperatures, allowing solute clusters to grow and evolve more extensively. When the temperature drops below 400 K, the vacancy gets trapped by these large clusters, and the evolution of cluster configurations and the total energy almost stops. As a result, the distribution of cluster sizes in the case with a slower cooling rate is more likely to resemble that of the constant-temperature kMC simulations conducted at higher temperatures.

The same situations happen to the distribution of the chemical concentration of solute clusters as well. Fig. 11(h) shows the correlation between the cluster size (X-axis) and the Zn/Mg ratio in clusters (Y-axis) for different cooling rates (red markers for WQ100, purple for WQ200, brown for WQ300 and gray for WQ500 cases, respectively).

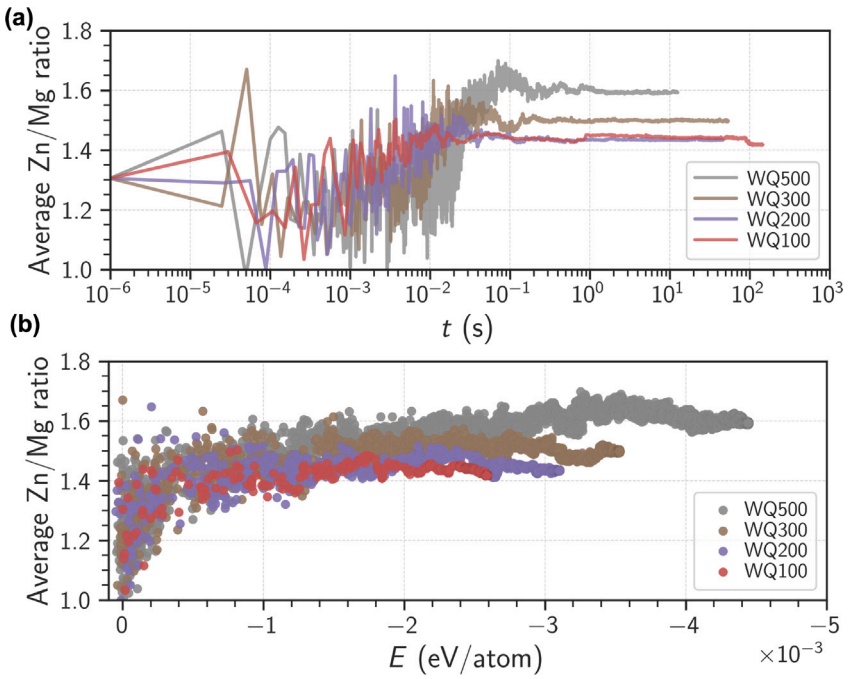

Fig. 12. Evolution of the average Zn/Mg ratio for clusters with a size larger than 10 clustered atoms in revised kMC simulations with different temperature evolution profiles defined in Fig. 1(b): WQ100 (red), WQ200 (purple), WQ300 (brown), and WQ500 (gray). (a): The time evolution of the average Zn/Mg ratios in these clusters. (b): The relation between the average Zn/Mg ratio in these clusters and the average energy per atom of the whole supercell relative to the initial solid solution state. (For interpretation of the references to color in this figure legend, the reader is referred to the web version of this article.)

Clusters with sizes smaller than 10 atoms show a wide range of Zn/Mg ratios. For larger solute clusters (sizes greater than 10 atoms), most of the clusters exhibit a Zn/Mg ratio from approximately ~1.0 to ~2.0. The Zn/Mg ratio distributions fall within more narrow ranges as the cooling rates get slower. This change implies that the slower cooling rate promotes the average size of solute clusters as well as a more uniform and consistent Zn/Mg atomic ratio of the clusters. Fig. 11(i) shows the kernel density estimations of the Zn/Mg ratio of clusters with the weight of cluster size for different cooling rates (red curve for WQ100, purple for WQ200, brown for WQ300, and gray for WQ500 cases, respectively). In this figure, the estimation curve of the WQ100 case shows a wider distribution with a peak value situated at approximately 1.39, with a standard deviation of $\sigma = 0.5$. This indicates that a majority of the aggregated atoms are clustered within this specific range. In the WQ200 cases, the peak becomes sharper with a smaller width, and the value for the peak of kernel density estimations is situated at approximately 1.48. As the cooling rates decrease, such as those in the WQ300 and WQ500 cases, the peaks are more evident, situated at approximately 1.51 and 1.60, respectively. This analysis also highlights a consistent trend in which the peak value of the curve (i.e. the most representative Zn/Mg ratio) increases as the simulation cooling rate declines, showing the characteristics of solute clustering kinetics observed in the constant-temperature kMC simulations at higher temperatures.

The averaged Zn/Mg ratio for clusters comprising more than 10 atoms in the revised kMC simulations for all time frames is shown in Fig. 12. The evolution of this ratio in relation to time is illustrated in Fig. 12(a), while Fig. 12(b) shows the ratio with respect to the total energy change. As shown in Fig. 12(a), the Zn/Mg ratio for all cases undergoes significant oscillations within the range of 1.0 to 1.4 during the initial stages (before $t = 10^{-3}$ s). Concurrently, aside from these random fluctuations, no significant upward or downward trend has emerged. The underlying reason for this behavior is that the temperature remains high at this point in the simulation (above 650 K), so the solute clustering has not yet taken place to a substantial degree due to strong entropic effects. At these moments, only a few large clusters can be found in the supercell and hence the ratio shows more oscillations due to fewer atoms. After the initial stages, the Zn/Mg ratios begin to rise, eventually reaching a value around ~ 1.4 for the WQ100 and WQ200 cases. It achieves higher values of ~ 1.5 for the WQ300 case and ~ 1.6 for the WQ500 case. During these growth stages, many clusters nucleate and grow until the simulation temperature gradually decreases towards 400 K, which also causes a reduction in the degree of oscillation observed in the Zn/Mg ratios. After these growth stages ($\sim 1 \times 10^{-2}$ seconds for the WQ100 case, $\sim 5 \times 10^{-2}$ seconds for the WQ200 case, $\sim 5 \times 10^{-1}$ seconds for the WQ300 case, and $\sim 5 \times 10^{-1}$ seconds for the WQ500 case, respectively), the Zn/Mg ratio values appear to cease evolving in the final steady-state stages. This observation corresponds to the same stage in the energy profile illustrated in Fig. 10(a), where the average energy per atom E of the whole supercell stops its evolution.

Fig. 12(b) provides more insightful information regarding the averaged Zn/Mg ratio during the intermediate growth stages in the revised kMC simulations. The values oscillate in the beginning when the average energy per atom E of the whole supercell is high, which corresponds to the initial stage of the quenching process. Then the averaged Zn/Mg ratio remains almost constant as the E values become more negative during cluster nucleation and growth. At these stages, the Zn/Mg ratio remains approximately ~ 1.4 for the WQ100 and WQ200 cases. This ratio, as observed in the revised kMC simulations, exhibits similarities with the outcomes of the kMC simulation conducted at a constant temperature of 500 K, as depicted by the orange curve in Fig. 5(b). Similarly, for WQ300 and WQ500 cases with slower cooling rates, the ratio reaches higher values of ~ 1.5 and ~ 1.6, respectively, which lies between outcomes of kMC simulations at constant temperatures of 500 K and 650 K shown in Fig. 5(b). These observations suggest that despite the rapid cooling processes from 800 K to 300 K according to our simulated temperature profiles in Fig. 1(d), the average Zn/Mg ratio bears a closer resemblance to the results obtained above 500 K in constant-temperature kMC simulations rather than those at 300 K, indicating the major events of cluster nucleation and growth occur when the temperature is between $\sim$ 500 K and $\sim$ 650 K.

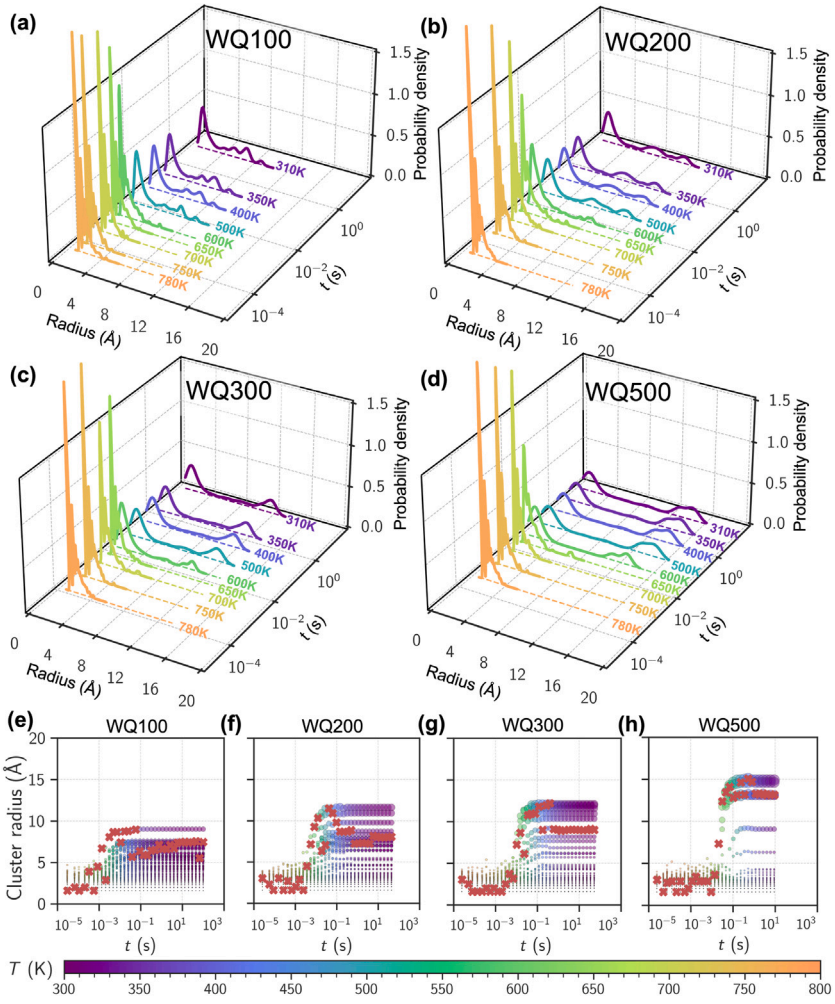

Fig. 13. Analyses for cluster size in terms of cluster radius in the revised kMC simulations with different temperature evolution profiles defined in Fig. 1(d). (a)–(d): Evolution of cluster radius at selected time points during WQ simulations, shown as a cluster size-weighted probability distribution function. Distribution curves are labeled and color-coded to indicate the simulation temperature at each time point. (e)–(h): Analyses for individual clusters across all time frames in the revised kMC simulations showing the correlations between the radius of clusters and simulation time. The color of the dots indicates the temperature (defined by the color bar at the bottom) at the corresponding simulation time. The size of the dots in the plots denotes the size of the clusters. Red crosses highlight the clusters that contain the vacancy at the corresponding simulation time. These subfigures share the same Y-axis ticks. (For interpretation of the references to color in this figure legend, the reader is referred to the web version of this article.)

The primary difference between the C300 simulation of infinite cooling rate and the WQ simulations lies in the behavior of the rapid nucleation kinetics at medium temperatures. Fig. 13 details the analysis results of the cluster radius defined by the size (number of atoms) on the Al lattice. Fig. 13(a)–(d) present the distributions of size-weighted probability function in different WQ simulations, ranging from single solute atoms to clusters larger than 10 Å in radius. The distribution reflects how solute atoms are aggregated into clusters of different sizes. Several distributions at selected times of different temperatures are plotted and colored based on the temperature. During the initial stage of the quenching, where the temperature is still high (>700 K), solute atoms mostly remain in the solution matrix. Occasionally, one or two small unstable clusters are observed (as the small peak of ~5 Å in Fig. 13(c) at 700 K), but these clusters are not stable and tend to dissolve quickly. Starting from ~650 K, the nucleation rates get accelerated. Stable nuclei can be observed in the simulation WQ500 of the slowest cooling rate (Fig. 13(d)). As the temperature decreases to 600 K, we begin to observe the formation of clusters around ~8 Å radius in WQ100 and WQ200 and clusters larger than 10 Å radius in WQ300 and WQ500. Notably, as the temperature further declines (<500 K), the size distribution in all simulations shows minor changes, likely due to the vacancy trapping effect within the clusters.

Despite this rapid cooling, which decreases from 800 K to 350 K at rates of approximately 2500 K/s for WQ100, 737 K/s for WQ200, and 346 K/s for WQ300, respectively, our observations distinctly capture the fast kinetics of cluster formation at intermediate temperatures. Due to rapid nucleation kinetics at medium temperature, the formation of precipitates in Al–Mg–Zn alloys possibly starts as early as during the quenching process. Different cooling rates, however, can lead to diverse distributions in the clustering of solute atoms after quenching. The simulation of WQ100 (Fig. 13(a)), which experiences the most rapid cooling, shows a final distribution of clusters that is quite similar to that observed in the 300 K constant temperature simulation (Fig. 6(a)). The largest size in WQ100 reaches ~9 Å radius. This implies that at the quickest cooling rate, the clusters do not grow significantly larger after they form, resulting in a final cluster size distribution with smaller, more numerous clusters. The cases with slower cooling rates, such as WQ200, WQ300, and WQ500, present a final distribution of large solute clusters (>~10 Å radius), similar to those from higher temperatures of 500 K and 650 K. This trend indicates that the slower cooling rate permits the solute atoms more time to migrate and form larger clusters, resulting in fewer but larger clusters. However, compared with constant-temperature kMC at higher temperatures, the cases of WQ200 and WQ300 show higher peaks in the regions of small clusters (<~10 Å radius), similar to the peak of small solute clusters of 300 K kMC in Fig. 6(a)). Thus, the cluster size distributions of these quenching cases behave as mixtures of those from constant-temperature kMC simulations at both low (~300 K) and high (≥ 500 K) temperatures.

To investigate the underlying vacancy-trapping mechanisms, the analysis of individual clusters extracted from different time frames of the simulation results derived from the WQ simulations is presented in Fig. 13(e)–(h), respectively. The color of each dot corresponds to the simulation temperature at the corresponding time frame according to the temperature evaluation profiles in Fig. 1(d), and the size of the dots represents the size of the corresponding cluster. In addition, some of the clusters are highlighted by red crosses in the figures, meaning these clusters contain a vacancy at that time. Fig. 13(e)–(h) display the relationship between the time when the clusters appear (X-axis) and the size of each cluster (Y-axis). During the initial stage of the quenching processes, the clusters remain relatively small until the temperature descends to around ~ 650 K: this is in alignment with the previous observations. This trend is evident in all WQ simulations. As the temperature continues to decrease, solute atoms increasingly tend to be aggregated and form larger clusters. In the WQ100 case, the largest cluster observed reaches ~9 Å radius, comprising approximately 200 atoms. In the WQ200 and WQ300 cases, the largest cluster is approximately ~12 Å radius, consisting of roughly 400 atoms, and the WQ300 case generates more large clusters than the WQ200 case. For the WQ500 case, the largest cluster found contains about 800 atoms and is about ~15 Å radius. We also observe that prior to reaching the aforementioned temperature threshold for the steady states (~ 400 K shown in Fig. 10(a)), the red crosses are not consistently present for all time frames in the figures. This implies that at higher temperatures, the diffusivity of the vacancy remains considerably high, and the vacancy may be situated within the Al matrix when the time frame is analyzed. However, once the simulation temperature descends to 400 K, the vacancy appears in nearly every subsequent time frame, indicating that it has been captured by the clusters. It is also worth noting that there are instances where the vacancy may escape from one cluster, but it is still highly likely to be captured again by another cluster shortly after the escape. The clusters that contain the vacancy (highlighted by red crosses) are not necessarily the ones with the largest cluster sizes as shown at the steady states in all WQ cases.

To further explain the vacancy trapping effect of clusters, we conducted a comprehensive analysis of clusters in Al–Mg–Zn, particularly regarding the clusters' vacancy binding energy, E_b^{cluster} and migration barriers E_m. The results, derived from kMC simulations and evaluated by surrogate models, are summarized in Fig. 14. Fig. 14(a)–(c) illustrate an example cluster extracted from the WQ500 simulation, sliced to show its internal structure. The color-coding within the cluster in Fig. 14(a) reveals the internal structure of Al, Mg, and Zn. This precipitate, clustered from the medium temperature, shows a similar atomistic structure as shown in Fig. 9(a), which is close to $L1_2$ but with numerous substitutional defects.

In Fig. 14(b), the spatial distribution of the local binding energy of each site, denoted as E_b^{local}, is depicted. This parameter is calculated from the following formula:

$$E_b^{\text{local}} = \left(E(\text{Vac}) - E\left(\text{Al}_{N-1}\text{Vac}\right)\right) - \min_{\text{X=Al,Mg,Zn}} \left(E(\text{X}) - E\left(\text{Al}_{N-1}\text{X}\right)\right) \quad (9)$$

Here, E(Vac) denotes the energy of the supercell cell that contains a cluster with a vacancy at a particular local site in this cluster, E(X) is the energy of the same supercell with an additional atom X to fill up the previous local vacancy site, $E(\text{Al}_{N-1}\text{Vac})$ is the energy of a large Al supercell with one vacancy, and $E(\text{Al}_{N-1}\text{X})$ is the energy of the same Al supercell with extra atom X to fill up this vacancy, respectively. Here the additional atom X can be Al, Mg, or Zn. The minimization in Eq. (9) following semi-grand canonical ensembles determines which atom type, among Al, Mg, and Zn, results in the lowest energy when it occupies the local site, regardless of the chemical potential of the atoms involved. This process reflects a thermodynamic preference of the site. The value of E_b^{local} quantifies the binding energy of a vacancy at a specific site in comparison to the most thermodynamically preferred element for that site. When the vacancy is in the dilute Al matrix, $E_b^{\text{local}} \approx 0$, indicating no additional binding for the vacancy. However, when the vacancy is within a cluster, E_b^{local} typically shows a negative value which indicates that the vacancy is more likely to be bound or 'trapped' within the cluster compared to being in the Al matrix. It serves as an indicator of the energetic difference between a given site and that of pure aluminum. The radial distribution of this energy of atoms in the cluster and surrounding Al atoms in the matrix is shown in Fig. 14(d). As shown in Fig. 14(b) and (d), there are some sites (mostly Zn sites) inside the cluster that show quite negative E_b^{local}, which signifies a relatively stronger binding effect of the sites, indicating a site's propensity to attract a vacancy. There are also some positive E_b^{local} sites around the precipitate-matrix interface (dashed line in Fig. 14(d)), indicating less tendency to attract vacancies.

Fig. 14(c) and Fig. 14(e) show, respectively, the spatial and radial distribution of the local average migration barriers of each site, E_m^{local}, of the cluster. To obtain E_m^{local}, we assume that a vacancy occupies the local lattice site. This parameter represents the arithmetic mean of the 12 individual vacancy migration barriers, ΔE_a, which are computed using our surrogate model, to each of its 12 first nearest neighbor sites. The analysis indicates a prevalence of low-barrier sites within the cluster. Mg sites inside tend to have a lower value around ~ 0.3 eV. This is due to the fact that Zn atoms frequently constitute the first nearest neighbors to Mg in the Mg-Zn clusters. Given that Zn atoms generally exhibit a lower ΔE_a within Al–Mg–Zn alloys [9], this lower value significantly influences the energy landscape for migration barriers. Moreover, when accounting for the Arrhenius factor, $\exp\left(-\frac{\Delta E_a}{k_B T}\right)$, the effective migration barriers within the cluster become even lower.

To conclude the information from Fig. 14(b)–(e), we illustrate the energy profile of the binding effect in terms of the vacancy migration coordinate in Fig. 14(f). The energy basin shows the vacancy-trapping potential of a cluster. The landscape illustrates that the average vacancy migration barriers E_m, are lower within the cluster's domain, and exhibit higher values in the matrix as indicated by Fig. 14(c) and (e). The binding energy of the cluster to the vacancy, E_b^{cluster} is determined by the energy difference between the lowest energy state (vacancy trapped by the cluster) and the untrapped state (vacancy in the matrix). It is noteworthy that while certain sites at the cluster-matrix interface present positive local binding energies, the true vacancy migration energy profile should be multi-dimensional and inclined to traverse along paths of minimum energy.

To obtain a coarse-grained picture and reveal the general capacity of vacancy trapping in different clusters, the binding energy of a cluster, E_b^{cluster}, can be defined as the lowest energy state among all sites:

$$E_b^{\text{cluster}} = \min_{i \in \text{cluster}} E_b^{\text{local}}(i) \quad (10)$$

where the site i iterates over all sites in a cluster. Values of E_b^{cluster} for clusters of varying sizes are thoroughly studied. The clusters are derived from kMC simulations at constant temperatures (Fig. 14(g)) and from the simulations incorporating various cooling rates (Fig. 14(h)). No matter from which type of simulation the cluster formed, the evolving of E_b^{cluster} primarily follows the same trend. As indicated by these two figures, the evolution of E_b^{cluster} is characterized by two distinct stages. In the first stage, corresponding to the formation of small solute clusters with less than approximately 150 atoms, we observe that the clusters' capacity to trap vacancies (E_b^{cluster}) increases fast as the cluster size grows. Transitioning to the second stage, which occurs once clusters surpass a critical size threshold of approximately 150 atoms, the clusters begin to exhibit more ordered atomic structure. At this mature stage of cluster growth, we find that the vacancy trapping ability (E_b^{cluster}) becomes relatively insensitive to further increases in cluster size. Besides the correlation with clusters' size, the cluster binding energy, E_b^{cluster}, has a strong correlation with the average formation energy of cluster $\bar{E}_f$. See Supplementary Note 7 for more details.

Averaged E_m is defined as the arithmetic mean of the vacancy migration barriers, ΔE_a, of some specific types for the cluster. As

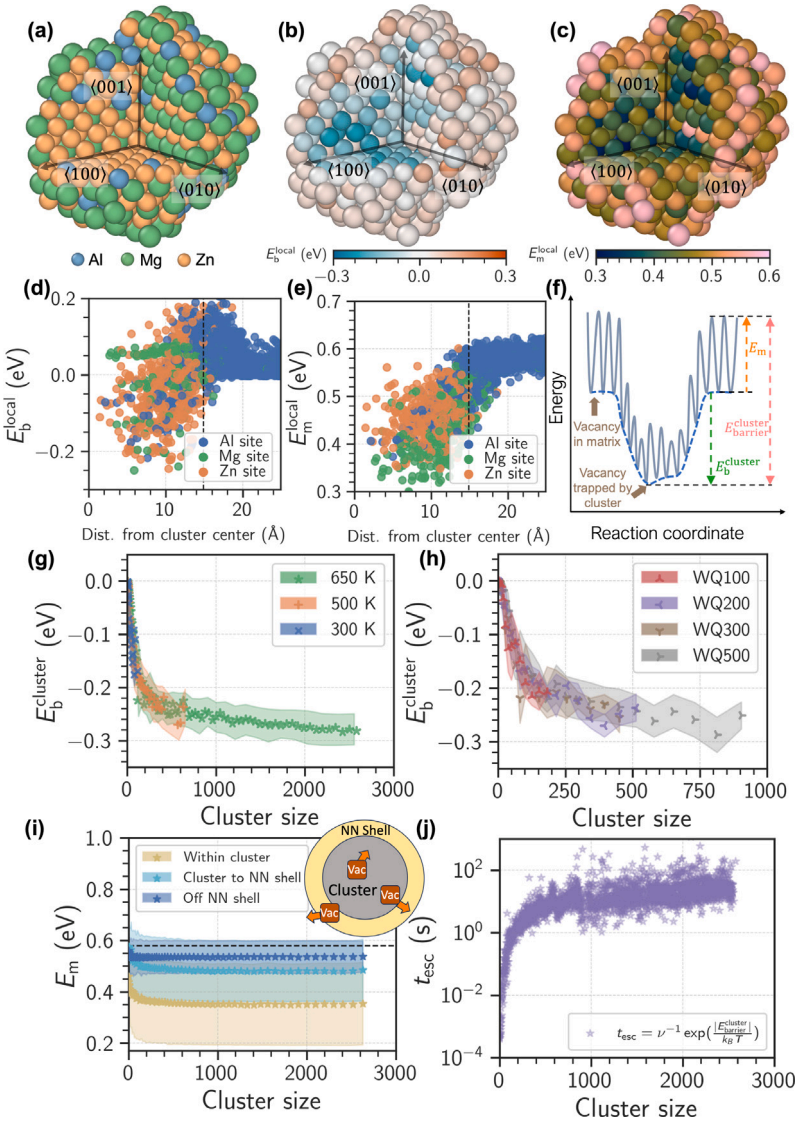

Fig. 14. Analyses of the vacancy trapping mechanisms by cluster vacancy binding energy $E_b^{cluster}$ and migration barriers E_m. (a)–(c) An example cluster formed from the WQ500 simulation showing the inner structures. The cluster is colored to show the spatial distribution of element type (a), the local vacancy binding energy of each site E_b^{local} (b), and the local average vacancy migration barrier E_m^{local} (c). (d)–(e): The radial distribution of the E_b^{local} (d) and E_m^{local} (e) of the cluster and surrounding Al matrix. Each dot represents a local lattice site, colored by the chemical type of atom that occupies this site. The black dashed line represents the radius of the cluster. (f): The conceptual illustration of the energy landscape in terms of vacancy migration coordinate inside and near a solute cluster. The dashed line connects local minima while the curved line connects both minima and transition states. $E_b^{cluster}$ is defined by Eq. (10) as the difference from the lowest energy state (vacancy trapped by cluster) to the untrapped state (vacancy in matrix). E_m denotes the averaged migration barriers. (g)–(h): Averaged $E_b^{cluster}$ for clusters of different sizes from the kMC simulations at constant temperature (g) and the revised kMC simulations during quenching with different cooling rates (h). (i) Averaged vacancy migration barrier E_m of different type for clusters of different sizes. Yellow stars mark the vacancy migration event inside clusters. Light blue stars denote the event vacancy jumping from the surface of the cluster to the nearest neighbor shell. Dark blue stars represent the event vacancy jumping out of the nearest neighbor shell. The horizontal dashed line denotes the vacancy migration barrier in pure Al of 0.58 eV. The shaded regions in (g)–(i) indicate the standard deviations. (j) Estimated vacancy escape time from a solute cluster, t_{esc}, calculated by Eq. (11). (For interpretation of the references to color in this figure legend, the reader is referred to the web version of this article.)

shown in the subfigure of Fig. 14(i), three types of vacancy migration events are presented, namely, vacancy migrating inside clusters, vacancy jumping from the surface of the cluster to the nearest neighbor shell, and vacancy jumping out of the nearest neighbor shell. Here, different types of averaged E_m for clusters of different sizes are studied. The evolution of E_m is also characterized by two stages. During the first stage, E_m drops slightly as cluster size grows. This trend stabilizes when the cluster size reaches a threshold of approximately 150 atoms, beyond which E_m remains relatively constant. Further, we analyzed three different types of vacancy migration events related to clusters as shown in the subfigure in the upper right. The first category is the type of vacancy migration within clusters (marked by yellow stars and shaded regions). Although this type shows a very large standard deviation of 0.18 eV, it has a low average of 0.37 eV. The second type colored by light blue denotes the event in which a vacancy jumps from the surface of the cluster to the nearest neighbor shell. It has a higher converged average of 0.50 eV and a smaller standard deviation of 0.13 eV. The third category is denoted by dark blue, representing the event in which a vacancy jumps out of the nearest neighbor shell. Notably, the vacancy is still affected by the cluster since it is still near the cluster. This type has an average of 0.54 eV and a standard deviation of 0.07 eV. This gradation of E_m of different types, shows a similar trend as shown in Fig. 14(e), that is an increase of E_m from the interior of the cluster to the surrounding Al matrix. It is important to note that once

a vacancy escapes the cluster's effective domain entirely, E_m should have a typical value of 0.58 eV, which is the value of ΔE_a in the Al matrix [97].

Finally, Fig. 14(j) displays the estimated vacancy escape time at $T = 300$ K by the equation:

$$t_{esc} = \nu^{-1} \exp\left(\frac{\left|E_{barrier}^{cluster}\right|}{k_B T}\right) \quad (11)$$

Within this equation, ν is the attempt frequency, set at 10^{13} Hz, the same as the value we applied in the kMC simulations. $E_{barrier}^{cluster} = E_m - E_b^{cluster}$ is the overall barrier as shown in Fig. 14(f). Note the negative sign is due to the negative value of $E_b^{cluster}$ when a vacancy is trapped by the cluster. Here, $E_b^{cluster}$ is obtained from the analysis presented in Fig. 14(g) and (h). E_m is specified as 0.58 eV, indicating the state in which vacancy escapes the cluster's effective domain entirely. As shown in Fig. 14(j), the general trend of t_{esc} as a function of cluster size can also be divided into two stages. In the initial stage, as cluster size increases, there is a sharp increase in vacancy escape time at a logarithm scale from 10^{-3} seconds to 1 s. Most of the clusters from the simulation C300 are within this stage, with a size smaller than 100 atoms. Vacancy escape time from these clusters is less than 1 s. As the cluster size reaches the threshold, a much slower increase is observed. During this stage, the vacancy escape time does not significantly change with increasing cluster size. As the size increases from 200 to 2500, t_{esc} grows much slower compared to the first stage. This implies that the vacancy trapping mechanism in the second stage becomes size-insensitive, and would finally converge to the value estimated from $E_b^{cluster}$ of the pure precipitate phase.

4. Discussion and conclusions

Our kMC framework represents a sophisticated approach for simulating the intricate dynamics of solute clustering, particularly focusing on the nucleation processes under various temperatures and the quenching rates based on real-world temperature evolution profiles. It has the capability to provide comprehensive insights into the size, density, chemical composition, and structural configurations of solute clusters throughout both the aging and quenching processes. Moreover, it is also capable of capturing the complex mechanisms of solute cluster nucleation and growth mechanisms at an atomic level. In addition, we adopted a Monte Carlo-based simulated annealing heuristic to evaluate the free-energy profile of Mg-Zn-rich clusters for Al–Mg–Zn alloys. We have successfully applied these free energies to the CNT model. As illustrated in Fig. 7, there is a great consistency and complementarity between the constant-temperature kMC simulation and CNT models, especially in describing solute clusters in terms of size, density, and Zn/Mg ratio during the nucleation stages. Furthermore, both the kMC and CNT have identified rapid nucleation kinetics when aging occurs at medium temperatures.

Due to the fast nucleation at medium temperature, we observed a rapid formation of large solute clusters at 500–600 K during the quenching from our revised kMC simulations. This observation is in line with our recent TEM study that captured solute clusters with ~ 2 nm diameters immediately after quenching [13]. Our study also highlights the significant influence of quenching rates on the formation and characteristics of solute clusters. We have discovered that the nucleation and early growth stages of precipitation in Al–Mg–Zn alloys are highly sensitive to the thermal history of the alloy. Specifically, slower cooling rates result in the formation of larger, less densely distributed clusters with higher Zn/Mg ratios. Conversely, rapid cooling rates lead to smaller, more densely distributed clusters with lower Zn/Mg ratios. The difference in Zn/Mg ratio of solute clusters and GP zones may lead to different final precipitates [98]: when the Zn/Mg ratio is higher, GP zones are mainly transformed into η' and η phases ($MgZn_2$). When the Zn/Mg ratio is lower, GP zones may transformed into T' or T phases ($Mg_{32}(Al, Zn)_{49}$ or $Mg_3Zn_3Al_2$) [99]. This insight is invaluable for alloy designers and manufacturers to achieve specific microstructural characteristics in age-hardened alloys by controlling the cooling rate of a 7XXX Al alloy.

There have been many studies on vacancy-trapping mechanisms to affect solute clustering and aging kinetics [10–12,100]. For example, some trace solute elements, such as Sn [11,12,100], can have appropriate binding strengths with vacancies suggested by DFT calculations to effectively impede the solute diffusion and natural aging at room temperature. However, these vacancy-solute binding energies were calculated based on the direct interactions between a vacancy and one or several Sn atoms without considering the effects of large-size solute clusters as shown in Fig. 11. To consider this size effect, Zurob et al. [10] proposed a mechanism that suggests the binding strengths to a vacancy is proportional to the cluster size (the number of solute atoms in a cluster n): $t_{esc} \propto \exp(\frac{\alpha n E_b}{k_B T})$, where E_b is the solute vacancy binding energy and α is a fitted constant.

The evaluation of the vacancy-trapping effect of an ordered precipitate, such as Cu clusters in α-Fe, should be based on the difference between the vacancy formation energy in the matrix ($E_f^{vac,matrix}$) and the vacancy formation energy in the bulk precipitate phase ($E_f^{vac,precipitate}$) [87,88]. However, this evaluation method of the vacancy-trapping effect becomes particularly challenging when dealing with precipitates that have complex structures and varying non-stoichiometric compositions during solute clustering kinetics. To overcome this challenge, Jain et al. [101] estimate the cluster binding energy by examining the difference in cluster formation energy between clusters with and without a captured vacancy based on cluster configurations obtained directly during kMC simulations. This direct method inspired us to propose the vacancy binding energies defined by Eq. (9) and Eq. (10) for a particular cluster obtained directly from our kMC simulations.

In our work, we utilized static methods and established a correlation between the size of solute clusters and their binding effects, as illustrated in Fig. 14. We show the general tendencies of two different stages of vacancy trapping mechanism from the simulations. In the first stage, when the solute clusters are small (< 150 atoms), the trapping energy increases almost linearly with the cluster size. This observation aligns with the findings of Zurob et al. [10]. Specifically, single Zn and Mg atoms exhibit vacancy binding energies of −0.05 eV and −0.01 eV, respectively, in the Al matrix [102], but the vacancy binding energy of one solute cluster is just ~−0.2 eV when the cluster size reaches ~100 atoms, suggesting a relatively modest value for the parameter α in Zurob's model [10]. In the second stage, once the cluster reaches a critical size (> 150 atoms), clusters begin to exhibit more ordered atomic structures. At this mature stage of cluster growth, the trapping ability becomes relatively insensitive to further increases in cluster size. The vacancy binding energy gradually converges to ~-0.3 eV. This value could be determined by the structures and compositions of the bulk precipitate phase at equilibrium states [87,88]. Most of the clusters formed from the simulation C300 are small and in the first stage, their ability to trap vacancies is extensive to the cluster size. Hence the vacancy tends to jump among those largest clusters (Fig. 6(d)). On the other hand, numerous clusters from the WQ simulations are within the second stage, and their vacancy-trapping ability is more intensive. Thus, as clearly shown in Fig. 13, the vacancy is not necessarily trapped in those largest clusters.

At the next steps, our simulation framework based on the combination of the surrogate models of vacancy migration energetics ($\Delta E_a/\Delta E$) and the revised kMC algorithm can be directly used to investigate how the alloying compositions and temperature evolution profiles can affect the solute clustering during quenching and the early stages of natural aging when all the solute clusters are sill in the coherent lattice [13]. For example, it is important to investigate how the vacancy trapping mechanism would vary under the influence of a third solute element, such as Sn showing a solute-vacancy binding energy of −0.24 eV [102], which is regarded as a solute element that can effectively bind vacancies to impede the clustering kinetics at room temperatures in 6XXX

series Al–Mg–Si alloys [11,12,103]. The vacancy binding energy of small Mg-Si clusters in Al–Mg–Si are typically around −0.3 eV and may reach up to −0.5 eV for large clusters [101]. By comparison, the binding energy of Mg–Zn-rich clusters in Al–Mg–Zn atoms converges only up to −0.3 eV for clusters larger than 150 atoms. Hence, it suggests that Sn may have a different performance to affect natural aging in 7XXX series Al–Mg–Zn alloys since the Sn-vacancy binding is relatively stronger compared with most solute clusters in Al–Mg–Zn alloys. In addition, using the solute cluster configurations generated in our simulations and the appropriate interatomic potentials [104–106], it is possible to investigate how the heterogeneous distributions of solute clusters generated during quenching under different temperature evolution profiles can affect the dislocation activities by interactions with these solute clusters and the related mechanical properties.

Furthermore, the revised kMC simulations should be further improved to accurately capture the events that occur after the vacancy becomes trapped, where the mean vacancy migration barriers are lower, requiring a greater number of simulation steps to achieve the same time progression. The large energy basins created by these low-energy clusters demand more attempts for the vacancy to escape. There are already several advanced kMC algorithms that can potentially accelerate the simulations by addressing these challenges. For instance, the local super basin method [107,108] and hybrid kMC [109] can accelerate the process by solving the Markov chain more efficiently. Simulations with larger temporal and spatial resolutions, such as phase-field simulations, could also benefit from incorporating the heterogeneous distribution of size and chemical composition of clusters as inputs for studying natural aging processes. By accounting for the non-uniform distribution of clusters that arise from rapid quenching, these simulations can better capture the complex dynamics and interactions between solute atoms, vacancies, and clusters during natural aging.

In summary, the major conclusions of this study are:

1. KMC simulations at constant (aging) temperatures, following an infinite cooling rate quench after solutionizing, were performed using the above surrogate models of ΔE_a and ΔE to simulate solute clustering starting from a random solid-solution state in an Al–Mg–Zn alloy. These simulations reveal that rapid solute clustering occurs at medium temperatures, ranging from 500 K to 650 K. At 500 K, the diameter of clusters reaches around 2 nm in approximately 1 ∼ 10 s. At a higher temperature of 650 K, the diameter increases to approximately 4 nm within a time span of 0.1 s. The results indicate that early-stage phase transitions already occur during the fast quenching process.
2. KMC simulations at constant (aging) temperatures, following an infinite cooling rate quench after solutionizing, also reveal that relatively large-size and high-density solute clusters are generated at a medium temperature (500 K) relative to those obtained from either high-temperature (650 K) or room-temperature (300 K) kMC simulations. In addition, solute clusters formed at higher temperatures exhibit higher Zn/Mg ratios. Our time-independent CMC simulations confirm that clusters formed at different temperatures thermodynamically prefer two different phases of Mg-Zn compounds of different structures and compositions, namely: $L1_2$-like high-temperature structure of $MgZn_3$ (with a great amount of substitutional Al atoms on Zn sites) and $L1_0$-like low-temperature structure of MgZn. This leads to the preference for cluster compositions at the various temperatures investigated in the kMC simulations.
3. Free energy landscapes of Mg–Zn-rich solute clusters as a function of the numbers of Mg and Zn atoms in the Al–Mg–Zn alloys are estimated by the Monte Carlo-based simulated annealing method. The energetics are applied to the models based on the classical nucleation theory (CNT). The CNT predictions are generally in good agreement with the kMC simulation results in terms of the nucleation rate and the size-dependent solute cluster compositions (the Zn/Mg ratio).
4. KMC simulations at constant temperatures cannot fully capture the complicated kinetics of processes involving temperature gradients such as quenching. Hence, a revised kMC algorithm that can update the time-dependent temperature was engaged to study fast solute clustering during quenching processes, whose temperature evolution profiles are obtained from COMSOL Multiphysics simulations. The proposed algorithm offers a more rigorous approach to studying temperature-changing processes, providing a better understanding of the complex kinetics of solute clustering during fast quenching.
5. Number, sizes, and compositions of solute clusters strongly depend on quenching rates determined by the quenching temperature evolution profiles. Clusters generated during slower cooling rates tend to exhibit characteristics associated with larger cluster sizes, lower formation energies per atom, and narrower distributions of Zn/Mg ratios. In addition, the average Zn/Mg ratios in these clusters formed in these simulated quenching processes are always similar to the Zn/Mg ratio obtained from constant temperature kMC simulations conducted at higher temperatures (500 ∼ 650 K), indicating the main cluster nucleation and growth occurs rapidly at the intermediate temperature ranges. These distinct statistical features of the number, sizes, and compositions of solute clusters, depending on the quenching rates, provide different types of solute clusters as starting points (such as the heterogeneous nucleation sites) for subsequent natural aging processes.
6. Our revised kMC simulations demonstrate that the kinetics of solute clustering is significantly hindered in the quenching process as the temperature drops below ∼400 K. This occurs because of the trapping of vacancies by clusters exhibiting high absolute values of average formation energy per atom, rather than being solely influenced by clusters with the largest sizes. The solute clusters after the vacancy trapping reach steady states without significant changes in their structures, energies, or chemical compositions. The configurations of these steady-state clusters (average sizes and densities) are similar to the solute clusters we observed experimentally in 7XXX series Al alloy samples immediately after quenching [13], supporting the accuracy of our revised kMC simulations.
7. A vacancy trapping mechanism of two different stages is revealed. For small clusters, trapping energy rises nearly linearly with the cluster size [10]. Beyond a critical size (∼150 atoms), the vacancy trapping ability of clusters converges to ∼0.3 eV, insensitive to further size increases.

Declaration of competing interest

The authors declare that they have no known competing financial interests or personal relationships that could have appeared to influence the work reported in this paper.

Data availability

Data will be made available on reasonable request.

Acknowledgments

This research was supported by NSF-DMR-GOALI, Award No. 1905421. The calculations were performed by using the Extreme Science and Engineering Discovery Environment (XSEDE) Stampede2 at the TACC through Allocation No. TG-DMR190035.

Appendix A. Supplementary data

Supplementary material related to this article can be found online at https://doi.org/10.1016/j.actamat.2024.119795.

References

[1] S.P. Ringer, K. Hono, Microstructural evolution and age hardening in aluminium alloys: Atom probe field-ion microscopy and transmission electron microscopy studies, Mater. Charact. 44 (1–2) (2000) 101–131.

[2] Myriam Nicolas, Alexis Deschamps, Characterisation and modelling of precipitate evolution in an Al–Zn–Mg alloy during non-isothermal heat treatments, Acta Mater. 51 (20) (2003) 6077–6094.

[3] Emmanuel Clouet, Maylise Nastar, Christophe Sigli, Nucleation of Al 3 Zr and Al 3 Sc in aluminum alloys: From kinetic Monte Carlo simulations to classical theory, Phys. Rev. B 69 (6) (2004) 064109.

[4] Hiroshi Miyoshi, Hajime Kimizuka, Akio Ishii, Shigenobu Ogata, Temperature-dependent nucleation kinetics of Guinier-Preston zones in Al–Cu alloys: An atomistic kinetic Monte Carlo and classical nucleation theory approach, Acta Mater. 179 (2019) 262–272.

[5] Michel Perez, M. Dumont, Daniel Acevedo-Reyes, Implementation of classical nucleation and growth theories for precipitation, Acta Mater. 56 (9) (2008) 2119–2132.

[6] Yuri N. Osetsky, Laurent K. Beland, Roger E. Stoller, Specific features of defect and mass transport in concentrated FCC alloys, Acta Mater. 115 (2016) 364–371.

[7] Spencer L. Thomas, Srikanth Patala, Vacancy diffusion in multi-principal element alloys: The role of chemical disorder in the ordered lattice, Acta Mater. 196 (2020) 144–153.

[8] Yuri Osetsky, Alexander V. Barashev, Laurent K. Béland, Zhongwen Yao, Keyvan Ferasat, Yanwen Zhang, Tunable chemical complexity to control atomic diffusion in alloys, npj Comput. Mater. 6 (1) (2020) 38.

[9] Zhucong Xi, Mingfei Zhang, Louis G. Hector Jr., Amit Misra, Liang Qi, Mechanism of local lattice distortion effects on vacancy migration barriers in FCC alloys, Phys. Rev. Mater. 6 (7) (2022) 073601.

[10] H.S. Zurob, H. Seyedrezai, A model for the growth of solute clusters based on vacancy trapping, Scr. Mater. 61 (2) (2009) 141–144.

[11] S. Pogatscher, H. Antrekowitsch, M. Werinos, F. Moszner, S.S.A. Gerstl, M.F. Francis, W.A. Curtin, J.F. Loeffler, P.J. Uggowitzer, Diffusion on demand to control precipitation aging: Application to Al-Mg-Si alloys, Phys. Rev. Lett. 112 (22) (2014) 225701.

[12] M. Werinos, H. Antrekowitsch, T. Ebner, R. Prillhofer, W.A. Curtin, P.J. Uggowitzer, S. Pogatscher, Design strategy for controlled natural aging in Al-Mg-Si alloys, Acta Materialia 118 (2016) 296–305.

[13] Arya Chatterjee, Liang Qi, Amit Misra, In situ transmission electron microscopy investigation of nucleation of GP zones under natural aging in Al-Zn-Mg alloy, Scr. Mater. 207 (2022) 114319.

[14] Tolga Dursun, Costas Soutis, Recent developments in advanced aircraft aluminium alloys, Mater. Des. (1980-2015) 56 (2014) 862–871.

[15] Michael Minnicino, David Gray, Paul Moy, Aluminum Alloy 7068 Mechanical Characterization, Technical Report, Army Research Lab Aberdeen Proving Ground Md Weapons And Materials Research Directorate, 2009.

[16] I.N. Fridlyander, V.G. Sister, O.E. Grushko, V.V. Berstenev, L.M. Sheveleva, L.A. Ivanova, Aluminum alloys: Promising materials in the automotive industry, Metal Sci. Heat Treat. 44 (9–10) (2002) 365–370.

[17] Jürgen Hirsch, Aluminium in innovative light-weight car design, Mater. Trans. 52 (5) (2011) 818–824.

[18] Jürgen Hirsch, Recent development in aluminium for automotive applications, Trans. Nonferr. Met. Soc. China 24 (7) (2014) 1995–2002.

[19] Emad Scharifi, Victoria A Yardley, Ursula Weidig, Damian Szegda, Jianguo Lin, Kurt Steinhoff, Hot sheet metal forming strategies for high-strength aluminum alloys: A review–fundamentals and applications, Adv. Eng. Mater. 25 (2023).

[20] Daoming Li, Amit K. Ghosh, Biaxial warm forming behavior of aluminum sheet alloys, J. Mater Process. Technol. 145 (3) (2004) 281–293.

[21] Bernd-Arno Behrens, F. Nürnberger, Christian Bonk, S. Hübner, S. Behrens, H. Vogt, Influences on the formability and mechanical properties of 7000-aluminum alloys in hot and warm forming, J. Phys.: Conf. Ser. 896 (2017) 012004.

[22] J. Günzel, J. Haußß, P. Groche, Temperature-controlled tools for multi-stage sheet metal forming of high-strength aluminium alloys, IOP Conf. Ser.: Mater. Sci. Eng. 1157 (2021) 012086.

[23] Z.H. Cai, P. Batthyany, S. Dhawan, Q.L. Zhang, Y.H. Sun, X. Luan, L.L. Wang, M.M. Gharbi, Study of springback for high strength aluminium alloys under hot stamping, in: Advanced High Strength Steel and Press Hardening: Proceedings of the 4th International Conference on Advanced High Strength Steel and Press Hardening, ICHSU2018, World Scientific, 2019, pp. 117–121.

[24] Katherine E. Rader, Jon T. Carter, Louis G. Hector, Eric M. Taleff, Plastic deformation and ductility of AA7075 and AA6013 at warm temperatures suitable to retrogression forming, Metall. Mater. Trans. A 52 (2021) 4003–4017.

[25] Thomas A. Ivanoff, Eric M. Taleff, Louis G. Hector, Warm forming of aa7075-t6 with direct electrical resistance heating, Light Metals 2015 (2016) 223–227.

[26] Katherine E. Rader, Jon T. Carter, Louis G. Hector Jr., Eric M. Taleff, Retrogression forming and reaging of an AA7075-T6 alclad sheet material, J. Mater. Eng. Perform. 31 (7) (2022) 5311–5323.

[27] Johannes A. Österreicher, Georg Kirov, Stephan S.A. Gerstl, Ermal Mukeli, Florian Grabner, Manoj Kumar, Stabilization of 7xxx aluminium alloys, J. Alloys Compd. 740 (2018) 167–173.

[28] A. Deschamps, Y. Brechet, Influence of predeformation and ageing of an Al–Zn–Mg alloy—II. Modeling of precipitation kinetics and yield stress, Acta Mater. 47 (1) (1998) 293–305.

[29] Shengdan Liu, Chengbo Li, Suqi Han, Yunlai Deng, Xinming Zhang, Effect of natural aging on quench-induced inhomogeneity of microstructure and hardness in high strength 7055 aluminum alloy, J. Alloys Compd. 625 (2015) 34–43.

[30] A. Deschamps, G. Texier, S. Ringeval, L. Delfaut-Durut, Influence of cooling rate on the precipitation microstructure in a medium strength Al–Zn–Mg alloy, Mater. Sci. Eng. A 501 (1–2) (2009) 133–139.

[31] Gloria Graf, Petra Spoerk-Erdely, Peter Staron, Andreas Stark, Francisca Mendez Martin, Helmut Clemens, Thomas Klein, Quench rate sensitivity of age-hardenable Al-Zn-Mg-Cu alloys with respect to the Zn/Mg ratio: An in situ SAXS and HEXRD study, Acta Mater. 227 (2022) 117727.

[32] Hua-Ping Tang, Qu-Dong Wang, Chuan Lei, Bing Ye, Kui Wang, Hai-Yan Jiang, Wen-Jiang Ding, Xiang-Feng Zhang, Zhen Lin, Ji-Bin Zhang, Effect of cooling rate on microstructure and mechanical properties of an Al-5.0 Mg-3.0 Zn-1.0 Cu cast alloy, J. Alloys Compd. 801 (2019) 596–608.

[33] Alfredo Dupasquier, R. Ferragut, M.M. Iglesias, Fiorenza Quasso, Vacancy-solute association in coherent nanostructures formed in a commercial Al-Zn-Mg-Cu alloy, Phys. Status Solidi C 4 (10) (2007) 3526–3529.

[34] L.K. Berg, J. Gjønnes, V. Hansen, X.Z. Li, M. Knutson-Wedel, D. Schryvers, L.R. Wallenberg, GP-zones in Al–Zn–Mg alloys and their role in artificial aging, Acta Mater. 49 (17) (2001) 3443–3451.

[35] A.K. Mukhopadhyay, Guinier-preston zones in a high-purity Al-Zn-Mg alloy, Philos. Mag. Lett. 70 (3) (1994) 135–140.

[36] V. Hansen, O.B. Karlsen, Y. Langsrud, J. Gjønnes, Precipitates, zones and transitions during aging of Al-Zn-Mg-Zr 7000 series alloy, Mater. Sci. Technol. 20 (2) (2004) 185–193.

[37] John Banhart, Matthew D.H. Lay, C.S.T. Chang, A.J. Hill, Kinetics of natural aging in Al-Mg-Si alloys studied by positron annihilation lifetime spectroscopy, Phys. Rev. B 83 (1) (2011) 014101.

[38] Zeqin Liang, Cynthia Sin Ting Chang, Christian Abromeit, John Banhart, Jürgen Hirsch, The kinetics of clustering in Al–Mg–Si alloys studied by Monte Carlo simulation, Int. J. Mater. Res. 103 (8) (2012) 980–986.

[39] A. Deschamps, F. De Geuser, Zenji Horita, S. Lee, G. Renou, Precipitation kinetics in a severely plastically deformed 7075 aluminium alloy, Acta Mater. 66 (2014) 105–117.

[40] Olivier Ragueneau, P. Tréguer, A. Leynaert, R.F. Anderson, M.A. Brzezinski, D.J. DeMaster, R.C. Dugdale, J. Dymond, G. Fischer, R. Francois, et al., A review of the Si cycle in the modern ocean: Recent progress and missing gaps in the application of biogenic opal as a paleoproductivity proxy, Glob. Planet. Change 26 (4) (2000) 317–365.

[41] Tsai-Fu Chung, Yo-Lun Yang, Bo-Ming Huang, Zhusheng Shi, Jianguo Lin, Takahito Ohmura, Jer-Ren Yang, Transmission electron microscopy investigation of separated nucleation and in-situ nucleation in AA7050 aluminium alloy, Acta Mater. 149 (2018) 377–387.

[42] Sigmund J. Andersen, Calin D. Marioara, Jesper Friis, Sigurd Wenner, Randi Holmestad, Precipitates in aluminium alloys, Adv. Phys.: X 3 (1) (2018) 1479984.

[43] Elisabeth Thronsen, Sohail Shah, Constantinos Hatzoglou, C.D. Marioara, Sigurd Wenner, Sigmund Jarle Andersen, Bjørn Holmedal, Randi Holmestad, The evolution of precipitates in an Al–Zn–Mg alloy, J. Mater. Res. Technol. 23 (2023) 5666–5680.

[44] Darko Simonovic, Marcel H.F. Sluiter, Impurity diffusion activation energies in Al from first principles, Phys. Rev. B 79 (5) (2009) 054304.

[45] Xuesong Xu, Jingxu Zheng, Zhi Li, Ruichun Luo, Bin Chen, Precipitation in an Al-Zn-Mg-Cu alloy during isothermal aging: Atomic-scale HAADF-STEM investigation, Mater. Sci. Eng. A 691 (2017) 60–70.

[46] Yi-Yun Li, Libor Kovarik, Patrick J. Phillips, Yung-Fu Hsu, Wen-Hsiung Wang, Michael J. Mills, High-resolution characterization of the precipitation behavior of an Al–Zn–Mg–Cu alloy, Philos. Mag. Lett. 92 (4) (2012) 166–178.

[47] Adrian Lervik, Elisabeth Thronsen, Jesper Friis, Calin Daniel Marioara, Sigurd Wenner, Artenis Bendo, Kenji Matsuda, Randi Holmestad, Sigmund Jarle Andersen, Atomic structure of solute clusters in Al–Zn–Mg alloys, Acta Mater. 205 (2021) 116574.

[48] Elisabeth Thronsen, Jonas Frafjord, Jesper Friis, Calin Daniel Marioara, Sigurd Wenner, Sigmund Jarle Andersen, Randi Holmestad, Studying GPI zones in Al-Zn-mg alloys by 4D-STEM, Mater. Charact. 185 (2022) 111675.

[49] Frédéric Soisson, C.S. Becquart, Nicolas Castin, Christophe Domain, Lorenzo Malerba, Edwige Vincent, Atomistic kinetic Monte Carlo studies of microchemical evolutions driven by diffusion processes under irradiation, J. Nucl. Mater. 406 (1) (2010) 55–67.

[50] F. Soisson, A. Barbu, G. Martin, Monte Carlo simulations of copper precipitation in dilute iron-copper alloys during thermal ageing and under electron irradiation, Acta Mater. 44 (9) (1996) 3789–3800.

[51] G. Sha, A. Cerezo, Kinetic Monte Carlo simulation of clustering in an Al–Zn–Mg–Cu alloy (7050), Acta Mater. 53 (4) (2005) 907–917.

[52] Shoichi Hirosawa, Tatsuo Sato, Junichi Yokota, Akihiko Kamio, Comparison between resistivity changes and Monte Carlo simulation for GP zone formation in Al–Cu base ternary alloys, Mater. Trans. JIM 39 (1) (1998) 139–146.

[53] Juan M. Sanchez, Francois Ducastelle, Denis Gratias, Generalized cluster description of multicomponent systems, Physica A 128 (1–2) (1984) 334–350.

[54] Emmanuel Clouet, Alain Barbu, Ludovic Laé, Georges Martin, Precipitation kinetics of Al3Zr and Al3Sc in aluminum alloys modeled with cluster dynamics, Acta Mater. 53 (8) (2005) 2313–2325.

[55] Emmanuel Clouet, Céline Hin, Dominique Gendt, Maylise Nastar, Frédéric Soisson, Kinetic Monte Carlo simulations of precipitation, Adv. Eng. Mater. 8 (12) (2006) 1210–1214.

[56] COMSOL AB, COMSOL multiphysics®, 2022.

[57] Graeme Henkelman, Blas P. Uberuaga, Hannes Jónsson, A climbing image nudged elastic band method for finding saddle points and minimum energy paths, J. Chem. Phys. 113 (22) (2000) 9901–9904.

[58] Graeme Henkelman, Hannes Jónsson, Improved tangent estimate in the nudged elastic band method for finding minimum energy paths and saddle points, J. Chem. Phys. 113 (22) (2000) 9978–9985.

[59] Daniel Sheppard, Rye Terrell, Graeme Henkelman, Optimization methods for finding minimum energy paths, J. Chem. Phys. 128 (13) (2008) 134106.

[60] A. Zunger, P.E.A. Turchi, A. Gonis, Statics and dynamics of alloy phase transformations, NATO ASI Ser. Ser. B, Phys. 319 (1994).

[61] A. Van der Ven, G. Ceder, M. Asta, P.D. Tepesch, First-principles theory of ionic diffusion with nondilute carriers, Phys. Rev. B 64 (18) (2001) 184307.

[62] Xi Zhang, Marcel H.F. Sluiter, Cluster expansions for thermodynamics and kinetics of multicomponent alloys, J. Phase Equilibria Diffusion 37 (2016) 44–52.

[63] Tian Xie, Jeffrey C. Grossman, Crystal graph convolutional neural networks for an accurate and interpretable prediction of material properties, Phys. Rev. Lett. 120 (14) (2018) 145301.

[64] Zhantao Chen, Nina Andrejevic, Tess Smidt, Zhiwei Ding, Qian Xu, Yen-Ting Chi, Quynh T. Nguyen, Ahmet Alatas, Jing Kong, Mingda Li, Direct prediction of phonon density of states with Euclidean neural networks, Adv. Sci. 8 (12) (2021) 2004214.

[65] Alfred B. Bortz, Malvin H. Kalos, Joel L. Lebowitz, A new algorithm for Monte Carlo simulation of ising spin systems, J. Comput. Phys. 17 (1) (1975) 10–18.

[66] M. Athenes, Pascal Bellon, G. Martin, Identification of novel diffusion cycles in B2 ordered phases by Monte Carlo simulation, Phil. Mag. A 76 (3) (1997) 565–585.

[67] M. Athenes, P. Bellon, G. Martin, Effects of atomic mobilities on phase separation kinetics: A Monte-Carlo study, Acta Mater. 48 (10) (2000) 2675–2688.

[68] D.R. Mason, R.E. Rudd, A.P. Sutton, Stochastic kinetic Monte Carlo algorithms for long-range Hamiltonians, Comput. Phys. Commun. 160 (2) (2004) 140–157.

[69] Martin Volmer, A. Weber, Keimbildung in übersättigten Gebilden, Zeitschrift für physikalische Chemie 119 (1) (1926) 277–301.

[70] Ladislaus Farkas, Keimbildungsgeschwindigkeit in übersättigten Dämpfen, Zeitschrift für physikalische Chemie 125 (1) (1927) 236–242.

[71] Richard Becker, Werner Döring, Kinetische behandlung der keimbildung in übersättigten dämpfen, Ann. Phys. 416 (8) (1935) 719–752.

[72] Julius Frenkel, A general theory of heterophase fluctuations and pretransition phenomena, J. Chem. Phys. 7 (7) (1939) 538–547.

[73] Ya B. Zeldovich, On the theory of new phase formation: Cavitation, Acta Physicochem., USSR 18 (1943) 1.

[74] Dimo Kashchiev, Nucleation, Elsevier, 2000.

[75] Ken Kelton, Alan Lindsay Greer, Nucleation in Condensed Matter: Applications in Materials and Biology, Elsevier, 2010.

[76] Emmanuel Clouet, Modeling of nucleation processes, 2010, arXiv preprint arXiv:1001.4131.

[77] Henry Wu, Tam Mayeshiba, Dane Morgan, High-throughput ab-initio dilute solute diffusion database, Sci. Data 3 (1) (2016) 1–11.

[78] Scott Kirkpatrick, C. Daniel Gelatt Jr., Mario P. Vecchi, Optimization by simulated annealing, science 220 (4598) (1983) 671–680.

[79] Nicholas Metropolis, Arianna W. Rosenbluth, Marshall N. Rosenbluth, Augusta H. Teller, Edward Teller, Equation of state calculations by fast computing machines, J. Chem. Phys. 21 (6) (1953) 1087–1092.

[80] Abdullah Sadiq, A new algorithm for the Monte Carlo simulation of spin-exchange kinetics of ising systems, J. Comput. Phys. 55 (3) (1984) 387–396.

[81] Kristen A. Fichthorn, W. Hh Weinberg, Theoretical foundations of dynamical Monte Carlo simulations, J. Chem. Phys. 95 (2) (1991) 1090–1096.

[82] Santiago A. Serebrinsky, Physical time scale in kinetic Monte Carlo simulations of continuous-time Markov chains, Phys. Rev. E 83 (3) (2011) 037701.

[83] Xuezhou Wang, Dongdong Zhao, Yijiang Xu, Yanjun Li, Modelling the spatial evolution of excess vacancies and its influence on age hardening behaviors in multicomponent aluminium alloys, Acta Mater. 264 (2024) 119552.

[84] Karin M. Carling, Göran Wahnström, Thomas R. Mattsson, Nils Sandberg, Göran Grimvall, Vacancy concentration in Al from combined first-principles and model potential calculations, Phys. Rev. B 67 (5) (2003) 054101.

[85] E. Vincent, C.S. Becquart, C. Domain, Solute interaction with point defects in α Fe during thermal ageing: A combined ab initio and atomic kinetic Monte Carlo approach, J. Nucl. Mater. 351 (1–3) (2006) 88–99.

[86] Yi Wang, Jian Yin, Xiangbing Liu, Rongshan Wang, Huaiyu Hou, Jingtao Wang, Precipitation kinetics in binary Fe–Cu and ternary Fe–Cu–Ni alloys via kMC method, Prog. Nat. Sci.: Mater. Int. 27 (4) (2017) 460–466.

[87] E. Vincent, C.S. Becquart, Cristelle Pareige, Philippe Pareige, C. Domain, Precipitation of the FeCu system: A critical review of atomic kinetic Monte Carlo simulations, J. Nucl. Mater. 373 (1–3) (2008) 387–401.

[88] Frédéric Soisson, Chu Chun Fu, Cu-precipitation kinetics in α-Fe from atomistic simulations: Vacancy-trapping effects and Cu-cluster mobility, Physi. Rev. B 76 (21) (2007) 1–12.

[89] Alexander Stukowski, Visualization and analysis of atomistic simulation data with OVITO–the Open Visualization Tool, Model. Simul. Mater. Sci. Eng. 18 (1) (2009) 015012.

[90] Hiroshi Miyoshi, Hajime Kimizuka, Akio Ishii, Shigenobu Ogata, Competing nucleation of single-and double-layer Guinier–Preston zones in Al–Cu alloys, Sci. Rep. 11 (1) (2021) 1–11.

[91] Taichi Kamijo, Hiroshi Fukutomi, A new theory of the homogeneous nucleation of a coherent precipitate, Phil. Mag. A 48 (5) (1983) 685–693.

[92] Atsuto Seko, Shigeto R. Nishitani, Isao Tanaka, Hirohiko Adachi, Eiichi F. Fujita, First-principles calculation on free energy of precipitate nucleation, CALPHAD 28 (2) (2004) 173–176.

[93] Atsuto Seko, Natsuki Odagaki, Shigeto R. Nishitani, Isao Tanaka, Hirohiko Adachi, Free-energy calculation of precipitate nucleation in an Fe-Cu-Ni alloy, Mater. Trans. 45 (7) (2004) 1978–1981.

[94] Koretaka Yuge, Atsuto Seko, Isao Tanaka, Shigeto R. Nishitani, First-principles study of the effect of lattice vibrations on Cu nucleation free energy in Fe-Cu alloys, Phys. Rev. B 72 (17) (2005) 174201.

[95] Jizi Liu, Rong Hu, Jialing Zheng, Yidong Zhang, Zhigang Ding, Wei Liu, Yuntian Zhu, Gang Sha, Formation of solute nanostructures in an Al–Zn–Mg alloy during long-term natural aging, J. Alloys Compd. 821 (2020) 153572.

[96] Yingxin Geng, Qi Song, Zhaorui Zhang, Yanlin Pan, Hongxiang Li, Yuan Wu, Huihui Zhu, Di Zhang, Jishan Zhang, Linzhong Zhuang, Quantifying early-stage precipitation strengthening of Al–Mg–Zn (-Cu) alloy by using particle size distribution, Mater. Sci. Eng. A 839 (2022) 142851.

[97] Shun-Li Shang, Bi-Cheng Zhou, William Y. Wang, Austin J. Ross, Xuan L. Liu, Yong-Jie Hu, Hua-Zhi Fang, Yi Wang, Zi-Kui Liu, A comprehensive first-principles study of pure elements: Vacancy formation and migration energies and self-diffusion coefficients, Acta Mater. 109 (2016) 128–141.

[98] Keda Jiang, Yanquan Lan, Qinglin Pan, Yunlai Deng, Effect of the Zn/Mg ratio on microstructures, mechanical properties and corrosion performances of Al-Zn-mg alloys, Materials 13 (15) (2020) 3299.

[99] Yan Zou, Xiaodong Wu, Songbai Tang, Qianqian Zhu, Hui Song, Lingfei Cao, Co-precipitation of T' and η' phase in Al-Zn-Mg-Cu alloys, Mater. Charact. 169 (2020) 110610.

[100] Xinren Chen, Jaber Rezaei Mianroodi, Chuanlai Liu, Xuyang Zhou, Dirk Ponge, Baptiste Gault, Bob Svendsen, Dierk Raabe, Investigation of vacancy trapping by solutes during quenching in aluminum alloys, Acta Mater. 254 (2023) 118969.

[101] Abhinav C.P. Jain, M. Ceriotti, W.A. Curtin, Natural aging and vacancy trapping in Al-6xxx, J. Mater. Res. (2023) 1–17.

[102] Jian Peng, Sumit Bahl, Amit Shyam, J. Allen Haynes, Dongwon Shin, Solute-vacancy clustering in aluminum, Acta Mater. 196 (2020) 747–758.

[103] Abhinav C.P. Jain, Daniel Marchand, Albert Glensk, M. Ceriotti, W.A. Curtin, Machine learning for metallurgy III: A neural network potential for Al-Mg-Si, Phys. Rev. Mater. 5 (5) (2021) 053805.

[104] Daniel Marchand, W.A. Curtin, Machine learning for metallurgy IV: A neural network potential for Al-Cu-Mg and Al-Cu-Mg-Zn, Phys. Rev. Mater. 6 (5) (2022) 053803.

[105] So Takamoto, Chikashi Shinagawa, Daisuke Motoki, Kosuke Nakago, Wenwen Li, Iori Kurata, Taku Watanabe, Yoshihiro Yayama, Hiroki Iriguchi, Yusuke Asano, et al., Towards universal neural network potential for material discovery applicable to arbitrary combination of 45 elements, Nature Commun. 13 (1) (2022) 2991.

[106] So Takamoto, Daisuke Okanohara, Qing-Jie Li, Ju Li, Towards universal neural network interatomic potential, J. Materiomics 9 (3) (2023) 447–454.

[107] Kristen A. Fichthorn, Yangzheng Lin, A local superbasin kinetic Monte Carlo method, J. Chem. Phys. 138 (16) (2013) 164104.

[108] Brian Puchala, Michael L. Falk, Krishna Garikipati, An energy basin finding algorithm for kinetic Monte Carlo acceleration, J. Chem. Phys. 132 (13) (2010) 134104.

[109] Craig Daniels, Pascal Bellon, Hybrid kinetic Monte Carlo algorithm for strongly trapping alloy systems, Comput. Mater. Sci. 173 (2020) 109386.